Neuron

NeuroResource

# Whole-Neuron Synaptic Mapping Reveals Spatially Precise Excitatory/Inhibitory Balance Limiting Dendritic and Somatic Spiking

## Highlights

- Open source software allows mapping of synapses across whole neurons
- Annotated database of >90,000 synapses reveals several scales of synaptic organization
- Analysis reveals local balance between E and I synapses in specific dendritic domains
- Computational modeling shows that local E/I balance restricts dendritic and somatic firing

## Authors

Daniel Maxim Iascone, Yujie Li, Uygar Sümbül, ..., Idan Segev, Hanchuan Peng, Franck Polleux

## Correspondence

idan.segev@mail.huji.ac.il (I.S.), hanchuan.peng@gmail.com (H.P.), fp2304@columbia.edu (F.P.)

## In Brief

Iascone et al. developed an open source software within Vaa3D to map the distribution and morphology of synapses across the dendritic arbor of mouse layer 2/3 cortical PNs. Reconstruction of >90,000 synapses and computational modeling reveal several scales of organization, including domain-specific local balance between E and I synaptic distribution.

Iascone et al., 2020, Neuron *106*, 566–578
May 20, 2020 
https://doi.org/10.1016/j.neuron.2020.02.015

CellPress

CellPress

Neuron

NeuroResource

# Whole-Neuron Synaptic Mapping Reveals Spatially Precise Excitatory/Inhibitory Balance Limiting Dendritic and Somatic Spiking

Daniel Maxim Iascone,[1,2,10] Yujie Li,[3,4,10] Uygar Sümbül,[3,5] Michael Doron,[6,7] Hanbo Chen,[3,4] Valentine Andreu,[8] Finola Goudy,[8] Heike Blockus,[1,2] Larry F. Abbott,[1,2] Idan Segev,[6,7,*] Hanchuan Peng,[3,9,*] and Franck Polleux[1,2,11,*]

[1]Department of Neuroscience, Columbia University, New York, NY, USA
[2]Mortimer B. Zuckerman Mind Brain Behavior Institute, Columbia University, New York, NY, USA
[3]Allen Institute for Brain Science, Seattle, WA, USA
[4]Department of Computer Science, University of Georgia, Athens, GA, USA
[5]Department of Statistics, Columbia University, New York, NY, USA
[6]Edmond and Lily Safra Center for Brain Sciences, The Hebrew University, Jerusalem, Israel
[7]Department of Neurobiology, The Hebrew University, Jerusalem, Israel
[8]Department of Biology, Barnard College, New York, NY, USA
[9]Southeast University – Allen Institute Joint Center for Neuron Morphology, Southeast University, Nanjing, China
[10]These authors contributed equally
[11]Lead Contact
*Correspondence: idan.segev@mail.huji.ac.il (I.S.), hanchuan.peng@gmail.com (H.P.), fp2304@columbia.edu (F.P.)
https://doi.org/10.1016/j.neuron.2020.02.015

## SUMMARY

The balance between excitatory and inhibitory (E and I) synapses is thought to be critical for information processing in neural circuits. However, little is known about the spatial principles of E and I synaptic organization across the entire dendritic tree of mammalian neurons. We developed a new open-source reconstruction platform for mapping the size and spatial distribution of E and I synapses received by individual genetically-labeled layer 2/3 (L2/3) cortical pyramidal neurons (PNs) *in vivo*. We mapped over 90,000 E and I synapses across twelve L2/3 PNs and uncovered structured organization of E and I synapses across dendritic domains as well as within individual dendritic segments. Despite significant domain-specific variation in the absolute density of E and I synapses, their ratio is strikingly balanced locally across dendritic segments. Computational modeling indicates that this spatially precise E/I balance dampens dendritic voltage fluctuations and strongly impacts neuronal firing output.

## INTRODUCTION

The spatial organization of synapses throughout the dendritic tree is a critical determinant of their integration properties and dictates the somatic firing patterns of individual neuronal subtypes (Gidon and Segev, 2012; Katz et al., 2009; Liu, 2004; Polsky et al., 2004). Within dendritic branches, clustered potentiation of excitatory and inhibitory (E and I) synaptic inputs underlies both circuit development and experience-dependent plasticity (Chen et al., 2012; Frank et al., 2018; Harvey and Svoboda, 2007; Kleindienst et al., 2011; Makino and Malinow, 2011). Recently there has been substantial progress toward mapping neuronal connectivity on multiple spatial scales (Hildebrand et al., 2017; Iacaruso et al., 2017; Meijering et al., 2016; Sigal et al., 2015). However, significant roadblocks remain in identifying basic principles of synaptic organization for individual neuronal subtypes (Dickstein et al., 2016; Fogarty et al., 2013; Helmstaedter, 2013; Kleinfeld et al., 2011), leaving important questions unanswered. Are there multiple spatial scales of E and I organization within neurons? Are there hotspots of enhanced synaptic connectivity? Is there a structural correlate of E/I balance within specific dendritic domains or individual dendritic segments? Finally, how does E and I synaptic organization characterizing a given neuronal subtype influence the dendritic and somatic firing properties of these neurons?

Comparing the distributions of E and I synapses within the same neuron is particularly important to determine the cellular logic of synaptic organization. At the circuit level, a precise balance of excitation and inhibition is critical for calibrating both global and fine-scale levels of activity throughout development and during adult function (Dorrn et al., 2010; Froemke, 2015; Marlin et al., 2015). In both the auditory and somatosensory cortex, the co-tuning of E and I conductances is set by experience-dependent refinement of intracortical inhibition (D'amour and Froemke, 2015; Higley and Contreras, 2006). An anatomical basis for E/I balance within individual neurons has also been observed in the visual cortex and CA1, where excitatory inputs onto pyramidal neurons (PNs) are continuously offset by somatic inhibition (Takahashi et al., 2016; Xue et al., 2014). A conserved ratio of the numbers of E/I synapses was observed throughout

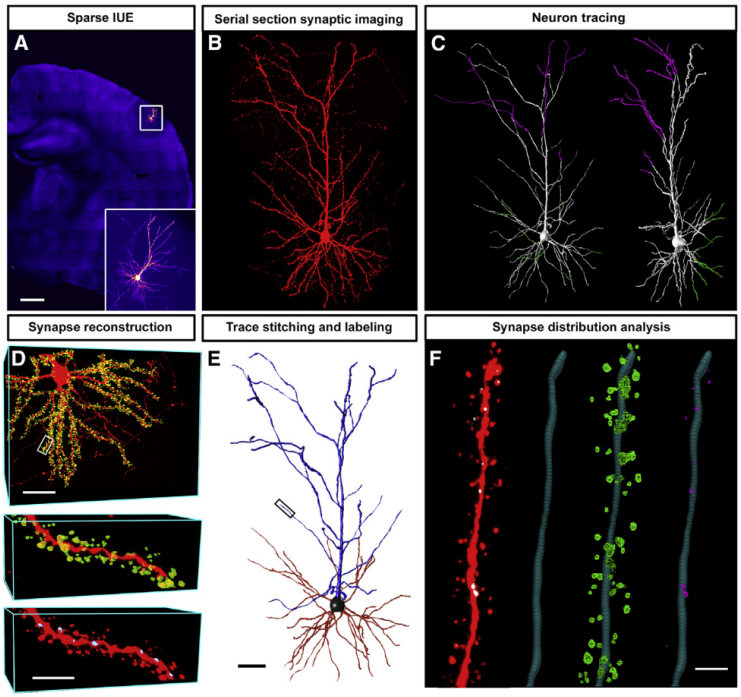


**Figure 1. Spatial and Morphological Annotation of Synapses across Whole Neurons with Synapse Detector**

(A) Sparsely labeled layer 2/3 pyramidal neuron (PN). Scale bar: 500 μm. Inset, higher magnification of the neuron shown.

(B) Single-synapse resolution image volume compiled from 3 adjacent tissue sections containing a complete layer 2/3 PN expressing tdTomato.

(C) Neuron trace of (B) (left) rotated to display the tissue section plane (right). Each color (magenta, silver, and green) represents a fragment of the dendritic arbor traced and stitched from adjacent tissue sections.

(D) Dendritic spines annotated throughout the basal dendritic arbor of (B) (top panel). Scale bar: 50 μm. Annotated spines (green in middle panel) and inhibitory Gephyrin-EGFP labeled synapses contained (blue in bottom panel) from the top panel inset. Scale bar: 5 μm.

(E) Neuron trace of (B) annotated with the Subtree Labeling program. Scale bar: 50 μm.

(F) From left to right: tdTomato volume from inset in (E) with identified inhibitory synapses labeled in white, corresponding trace, overlaid spine annotations, and inhibitory synaptic annotations associated with nodes within the trace. Scale bar: 2 μm.

the dendrites of cultured hippocampal neurons, suggesting that the spatial distribution of synapses might also contribute to E/I balance (Liu, 2004). However, this finding has not been extended to neurons *in vivo*. Activation of N-methyl-D-aspartate (NMDA)-type glutamate receptors leads to input-specific long-term potentiation of dendritic inhibition mediated by somatostatin-expressing interneurons, linking excitation and inhibition within individual dendritic segments (Chiu et al., 2018).

Here we have developed an adaptable open-source platform for imaging and mapping E and I synapses (ES and IS, respectively) across the entire dendritic arbor of individual neurons. We created whole-neuron reconstructions of individual, optically isolated PNs containing information about the size, shape, and continuous position of E and I synapses across their entire dendritic arbors: the first dataset of its kind for any neuronal subtype. We focused our study on layer 2/3 (L2/3) PNs of the adult mouse primary somatosensory cortex, where substantial prior knowledge of the synaptic microstructure and connectivity allowed validation of our platform and some of our findings (Ballesteros-Yáñez et al., 2006; DeNardo et al., 2015; Frangeul et al., 2016; Kubota et al., 2007; Lefort et al., 2009; O'Connor et al., 2010) as well as identification of new principles of E and I synaptic organization.

## RESULTS

### Synapse Detector: A Platform to Create Whole-Neuron Structural Input Maps

To obtain optically isolated complete L2/3 PNs for these synaptic reconstructions, we co-electroporated Cre-dependent FlextdTomato with low levels of Cre recombinase for extremely sparse *in utero* electroporation (Atasoy et al., 2008; Schnütgen et al., 2003) (Figure 1A; Video S1). We also labeled inhibitory synapses received by individual PNs by co-electroporating the inhibitory postsynaptic scaffolding protein Gephyrin tagged with EGFP, a strategy previously shown to reliably label GABAergic and glycinergic inputs without affecting their development (Chen et al., 2012; van Versendaal et al., 2012). We achieved single-synapse resolution (0.12 μm/pixel with 0.1 μm z-steps) with confocal microscopy by imaging neurons across 2–3 serial 150 μm vibratome sections with a 100× 1.49 NA objective lens (Figures 1B and 1D; Video S2).

This new Synapse Detector toolkit within Vaa3D generates synaptic maps by taking image data and a trace of the dendritic tree as input to automatically isolate E and I synapses within a user-defined radius of each dendrite. Within this toolkit, dendritic spines are classified with a Spine Detector module that identifies regions of fluorescence surrounding the dendritic trace (top and middle panels in Figure 1D; Videos S3, S4, and S5). Dendritic spines are the target of >90% of E synapses in the mammalian brain, including those targeting L2/3 PNs (Harris and Kater, 1994; Knott et al., 2006; Nimchinsky et al., 2002; Santuy et al., 2018b). More than 96% of spines in L2/3 PNs contain at least one postsynaptic density, and of those spines, >94% contain a single E synapse (Arellano et al., 2007; Santuy et al., 2018b). To validate the identification of dendritic spines as a structural proxy for E synapses in our system, we assessed the colocalization of Homer1c-tdTomato puncta with dendritic spines (Figures S2C–S2E). We found that ~90% of Homer1c puncta, a core

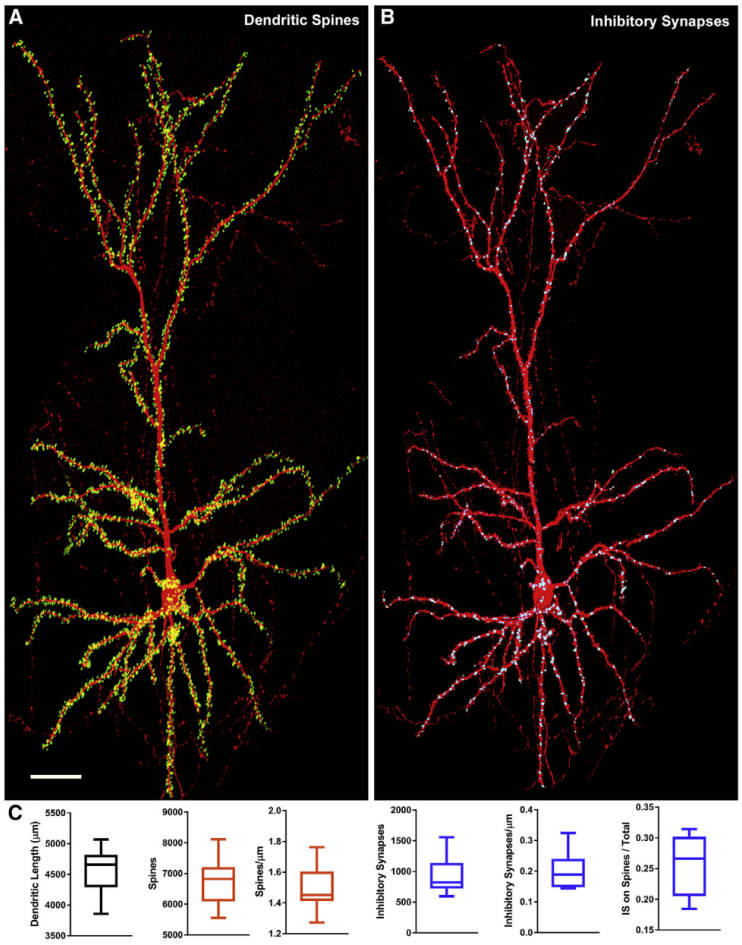


**Figure 2. Synaptic Distribution Profile for Layer 2/3 Somatosensory PNs**

(A and B) Example of complete reconstruction of 8,115 dendritic spines (green in A) and 1,045 I synapses (blue in B) throughout the dendritic tree of a single layer 2/3 PN (neuron 1; red cell filler, tdTomato). Scale bar: 50 μm

(C) From left to right: boxplots showing the distribution of dendritic length, dendritic spine number, dendritic spine density, inhibitory synaptic number, inhibitory synaptic density, and dually innervated spine proportions for all layer 2/3 PNs mapped in this study.

postsynaptic scaffolding component of excitatory synapses, were localized to dendritic spines compared to the dendritic shaft in L2/3 PNs (Hayashi et al., 2009; Usui et al., 2003).This observation confirms that, in mouse L2/3 PNs, the vast majority of excitatory synapses are made onto dendritic spines. Despite our observation that ~90% of E synapses onto L2/3 PNs target dendritic spines, the remaining 10% that target the dendritic shaft nonetheless represents a significant population of presynaptic inputs onto these cells and it will be interesting in future studies to explore their impact on dendritic integration.

Inhibitory synapses are identified using an IS Detector program that identifies EGFP-Gephyrin puncta that co-localize with cytosolic Flex-tdTomato (bottom panel in Figure 1D; Videos S1–S3). Together, these software modules measure the position of each E and I synapses throughout the dendritic tree in 3D as well as morphological features of E and I synapses such as their volume, spine neck length, and position of I synapses along dendritic shaft or on spine heads (so-called dually innervated spines) (Chen et al., 2012; Fossati et al., 2016; Kubota et al., 2007). During reconstruction, Synapse Detector's editing features allow the user to edit the volume of each identified synapse and eliminate false positives (Figure S1). Synapse Detector has a minimal false negative rate compared to manual reconstructions and generates consistent annotation results among multiple users (Figures S2J–S2M). Following reconstruction, synaptic features are associated with nodes, providing their geometric position in 3D along the dendritic tree. In the final step, neuron trace fragments from serial tissue sections containing information about the position and size of each synapse are stitched together into a final input map with the Vaa3D Neuron Stitcher program (Chen et al., 2017) (Figures S3–S5). This final synaptic input map can be used to analyze the morphology of all synapses as a function of their continuous distance from the soma along the dendritic arborization.

We used this new Vaa3D reconstruction pipeline to map E and I synapses across the dendritic arbor of ten PNs from L2/3 primary somatosensory cortex (as well as excitatory synapses from two additional PNs; Figure 2). These neurons contained on average 6,800 ± 212 dendritic spines (range: 5,575–8,187) and 979 ± 101 inhibitory synapses (range: 632–1,597; Figure 2C). On average, the total length of the dendritic trees we reconstructed was 4,579 ± 103 μm. These neurons displayed overall E and I synaptic densities consistent with previous reports of synaptic distribution from L2/3 PNs within the somatosensory cortex (1.48 ± 0.04 spines/μm and 0.20 ± 0.02 inhibitory synapses/μm, respectively) (Charrier et al., 2012; Chen et al., 2012; Fossati et al., 2016) (Figure 2C). We also found that 26% ± 2% of inhibitory synapses targeted dendritic spines in L2/3 PNs (Figure 2C). This fraction of spines dually innervated by an E and I synapse is comparable with previously observed values in these neurons (Chen et al., 2012; Fossati et al., 2016; Kubota et al., 2007). L2/3 PN spines have an average length of 1.121 ± 0.002 μm and an average volume of 0.267 ± 0.001 $\mu m^3$, while Gephyrin puncta have an average volume of 0.0493 ± 0.0005 $\mu m^3$ (Figures S3A–S3C). The distribution of all measured E synapse volumes (n = 81,604) conforms to a

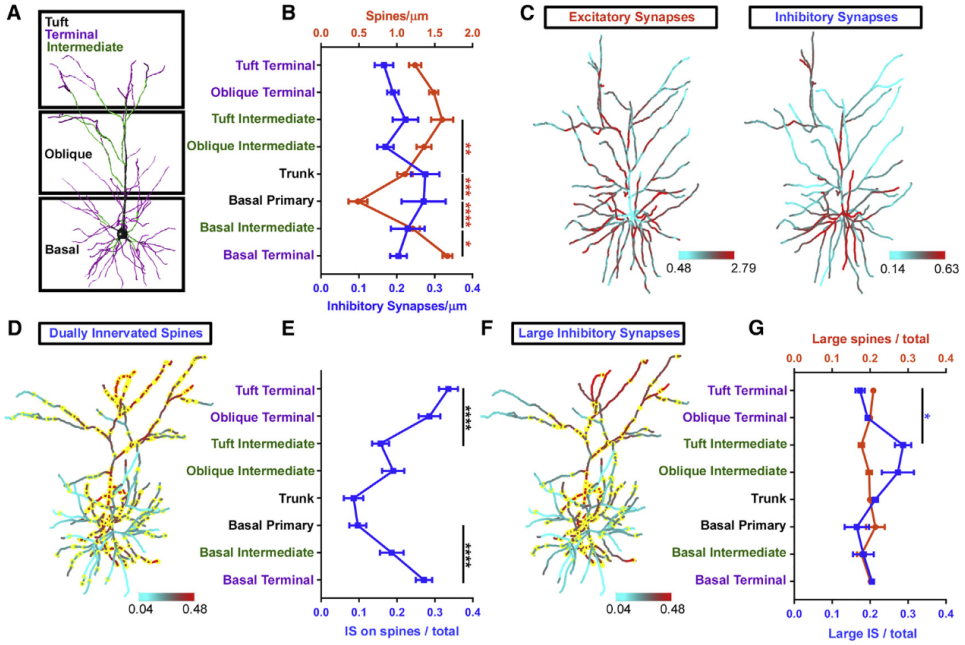


**Figure 3. Domain Organization of Synaptic Distribution and Morphology**

(A) A schematic diagram of a L2/3 PN depicting the domains (black boxes) and branch types (black, primary; green, intermediate; purple, terminal).

(B) The density of E (orange line) and I (blue line) synapses across dendritic branch types of L2/3 PNs.

(C) Heatmaps of E (left) and I (right) synaptic distribution indicating regions of low density (cyan) and high density (red).

(D) A heatmap of inhibitory synaptic distribution in which yellow puncta represent inhibitory synapses targeted to dendritic spines. Note the increased density of these dually innervated spines toward the distal apical tufts.

(E) The proportion of inhibitory synapses made onto dendritic spines across dendritic branch types.

(F) A heatmap of inhibitory synaptic distribution in which yellow puncta represent the 20$^{th}$ percentile of inhibitory synapses by volume for each domain type. Note the increased density of these large inhibitory synapses in apical intermediate segments.

(G) The proportion of large excitatory (orange) and inhibitory (blue) synapses across dendritic branch types.

For all plots, *p < 0.05, **p < 0.005, ***p < 0.001, and ****p < 0.0001. See STAR Methods for details. All data are presented as mean ± SEM.

log-normal distribution (Figure S3D). However, the distribution of all measured inhibitory synapse volumes (n = 9,798) shows a more complex distribution pattern, with a log-normal distribution for most inhibitory synaptic volumes (Figure S3G, right-hand side of graph) and another distribution of small inhibitory synaptic volumes (Figure S3G, left-hand side of graph) corresponding to inhibitory synapses made directly on spine heads. Compared with recent results (Santuy et al., 2018a), it may also be possible that we are slightly overestimating the volume of the 3%–5% smallest inhibitory synapses. It is unlikely that fixation could cause aggregation of cytosolic Gephyrin as our observations of inhibitory synaptic density are extremely similar to what has been observed *in vivo* in living mice (Chen et al., 2012). Interestingly, the distributions of E and I synaptic volumes are remarkably similar among individual neurons (total of twelve neurons for excitatory synapses and ten neurons for inhibitory synapses; Figures S3E, S3F, S3H, and S3I).

An important consideration for studies utilizing fluorescence microscopy to resolve fine structures such as synaptic morphology is the effect of light diffraction, whose limit is equal to the emission wavelength of the fluorophore divided by twice the numerical aperture of the objective lens (Conchello and Lichtman, 2005; Helmstaedter et al., 2008). For our reconstructions, this corresponds to a lateral diffraction limit of ~200 nm, allowing us to resolve >98% of excitatory synapses observed in somatosensory L3 by electron microscopy (Santuy et al., 2018a). Furthermore, to separate closely adjacent structures that might be incorrectly categorized as a single synapse, we used an adapted watershed algorithm that estimates boundary locations by measuring volume outward iteratively from the brightest voxels in the center of each identified structure (Barnes et al., 2014) (Figure S2G; see STAR Methods). We found that for L2/3 PNs within the somatosensory cortex, we are able to observe E and I synaptic densities that closely match estimates from studies utilizing serial scanning electron microscopy (Alonso-Nanclares et al., 2004; de Vivo et al., 2017; Knott et al., 2006) (Figures 2C and 3B). Additionally, after accounting for tissue shrinkage resulting from dehydration and fixation for electron microscopy, the distributions of E and I synaptic morphology we observed were well within the ranges reported using serial scanning electron microscopy (DeFelipe et al., 2002; Mollenhauer, 1993; Santuy et al., 2018a; Spacek and Hartmann, 1983) (Figure S3).

### Features of E and I Synaptic Organization across the Entire Dendritic Tree of L2/3 PNs

To analyze synaptic distribution across the fully reconstructed L2/3 PNs, we subdivided their dendritic arbors into four domains based on their morphology and distinct E and I input patterns: apical tuft, apical oblique, apical trunk, and basal dendrites (Spruston, 2008) (Figure 3A). L2/3 PNs receive perisomatic inhibitory inputs from parvalbumin-expressing basket interneurons and dendritically targeted inhibitory inputs from both somatostatin-expressing Martinotti interneurons and non-VIP interneurons expressing the serotonin receptor 5HT3a (Jiang et al., 2015; Tremblay et al., 2016). L2/3 PNs receive excitatory inputs predominantly from other L2/3 PNs and L4 spiny stellate neurons almost exclusively onto basal and apical oblique dendrites, while their apical tuft dendrites branching in L1 receive thalamic input from the posterior medial nucleus (POm) (DeNardo et al., 2015; Feldmeyer, 2012; Feldmeyer et al., 2002; Frangeul et al., 2016; Lübke et al., 2000). Within these dendritic domains, we distinguished among segment types by their relative branch order: primary, intermediate, and terminal (Spruston, 2008) (Figure 3A). This categorization is functionally relevant as different branch orders have distinct passive conductance properties resulting from their relative size and distance to the soma (Spruston, 2008; Vetter et al., 2001). Primary dendrites have relatively low input impedance due to their large size, while terminal dendrites have higher input impedance due to their smaller diameter and sealed end.

In addition to the domain classification used here, we developed a Subtree Labeling program as part of the Spine Detector toolkit, which enables user-directed annotation of regions of interest throughout the neuron trace to assess experiment-specific questions about domain-level synaptic organization (Figure S1E; see STAR Methods).

This division of the dendritic tree into specific domains and branch types allowed us to characterize the profile of synaptic distribution across L2/3 PNs. Similar to previous observations in CA1 PNs, E and I synaptic distribution appear to be inversely correlated at the domain level with relatively low spine density proximal to the soma, suggesting that this may be a general feature of synaptic organization across PN subtypes (Bloss et al., 2016; Megías et al., 2001) (Figure 3B). In contrast to previous studies, however, our complete reconstructions enable whole-neuron mapping of relative E and I synaptic distribution (Figures 2C, S4, and S5). Maps of E and I synaptic distribution in individual neurons demonstrated an almost complete absence of spines along primary dendrites accompanied by the highest density of inhibitory synapses (Figure 3C).

L2/3 PNs receive direct thalamic inputs from both the ventral posteromedial nucleus (VPM) and the POm terminating mainly onto their apical tufts (L1) and basal dendrites (L3), respectively (DeNardo et al., 2015; Petreanu et al., 2009). The vast majority of neocortical spines that are dually innervated by an inhibitory synapse receive excitatory inputs from thalamocortical axons, suggesting that distal tuft and basal dendrites should have a relatively high proportion of dually innervated spines (Kubota et al., 2007). Our unbiased mapping of the location of IS located on spine heads demonstrates that apical tuft and basal terminal dendrites of L2/3 PNs display a significantly higher proportion of dually innervated spines than primary and intermediate dendrites (Figures 3D and 3E), validating the spatial resolution of our labeling, imaging, and reconstruction approaches.

Because spine head volume is linearly proportional to excitatory synaptic strength (e.g., size of the post-synaptic density and density of glutamatergic α-amino-3-hydroxy-5-methyl-4-isoxazolepropionic acid (AMPA) receptors), it is also possible to use Synapse Detector to map the distribution of relative synaptic strengths (Katz et al., 2009; Pennacchietti et al., 2017; Schikorski and Stevens, 2001). We classified "large" synapses as greater than the highest $20^{th}$ percentile of synaptic volume for each neuron, closely corresponding to the persistent 60% increase in volume reported for synapses following structural forms of long-term potentiation (Harvey and Svoboda, 2007; Matsuzaki et al., 2004; Petrini et al., 2014). Interestingly, while there is no specific trend for the distribution of large spines across dendritic domains, large inhibitory synapses appeared to be clustered around the apical intermediate dendritic segments (Figures 3F and 3G), a feature never detected before.

### E and I Synaptic Distribution Is Structured and Locally Balanced within Dendritic Segments

Active dendritic conductances evoked by clustered synaptic inputs can produce nonlinear depolarization and change the probability of somatic firing (Losonczy et al., 2008). Local increases in excitatory synaptic density in a subset of segments within the same dendritic domain could reflect clustered spine stabilization following branch-specific synaptic potentiation (Harvey and Svoboda, 2007; Losonczy et al., 2008). Therefore, we tested if L2/3 PNs exhibit local changes in the relative distribution of E and I synapses across segments within each dendritic domain (Figure 4). To assess the extent of this potential weighted synaptic distribution, we compared the experimentally observed variation in synaptic density among segments within each dendritic domain to randomly shuffled synaptic densities for each neuron reconstructed. This was done by randomly redistributing synapses across segments within the same domain (see STAR Methods). Neurons in which synaptic distribution is significantly weighted toward a subset of dendritic segments would therefore display greater domain-specific variation in synaptic density than a randomized distribution of the same synapses across those segments. Excitatory synaptic (spine) distribution is significantly weighted toward a subpopulation of dendritic segments across almost the entire dendritic tree (Figures 4A and 4D). Interestingly, I synapses displayed significantly clustered distribution in only apical and basal terminal domains, raising the intriguing possibility that E and I synapses are weighted toward the same dendritic segments (Figures 4B and 4D).

Co-regulation of E and I synaptic inputs, generally referred to as E/I balance, is a critical mechanism for calibrating both global and fine-scale levels of neuronal activity (Haider and McCormick, 2009; Isaacson and Scanziani, 2011; Xue et al., 2014). While several studies have demonstrated mechanistic links between E and I synaptic potentiation, whether it results in local fine-scale balance between E and I synaptic distribution within dendritic segments remains an open question (Bourne and Harris, 2011; Chiu et al., 2018; Petrini et al., 2014). Interestingly, we found that E and I synaptic density strongly co-varied in

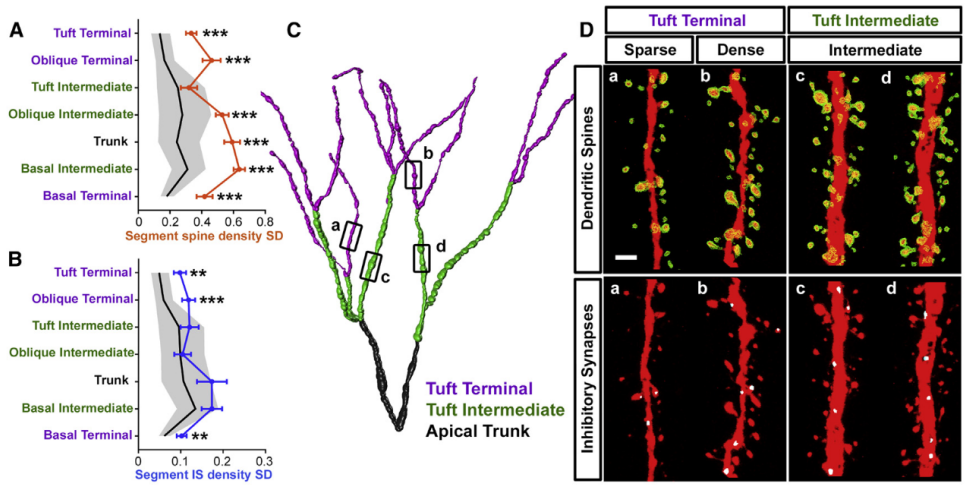


**Figure 4. Structured Synaptic Distribution within Branch Types**

(A) Variation in excitatory synaptic density (orange) across dendritic branch types of L2/3 PNs compared to 10,000 randomizations of each synaptic distribution within the same domains ($5^{th}$ to $95^{th}$ percentiles, gray).

(B) Variation in inhibitory synaptic density (blue) across dendritic branch types of L2/3 PNs compared to randomized synaptic distributions (gray).

(C) Example trace of apical tuft dendrites depicting the breakdown of the arbor into branch types (trunk, black; intermediate, green; terminal, purple).

(D) Excitatory (top) and inhibitory (bottom) synapses from segments isolated from the dendritic arbor in (C). Terminal tuft segments (left) display significant variation in E and I synaptic density while intermediate tuft segments (right) do not. Scale bar: 1 μm. For all plots, *$p < 0.05$, **$p < 0.005$, and ***$p < 0.001$. See STAR Methods for details. All data are presented as mean ± SEM.

terminal segments throughout the dendritic tree of L2/3 PNs (Figure 5). This structural E/I balance appears to increase as a function of distance from the soma, with segments distal to the soma showing a significant correlation between E and I synaptic density (Figure 5A). This local balance between E and I synaptic density on terminal segments remains significant even after dually innervated spines are removed from the analysis (Figures S3J and S3K). Taken together, these results demonstrate that, in L2/3 PNs: (1) both E and I synaptic density vary more than predicted by chance among dendritic segments within dendritic domains and (2) despite this weighted distribution of E and I synapses, the ratio between E and I synaptic density is tightly controlled locally within these segments.

## Functional Implications of Global and Domain-Specific E/I Balance

To better understand the functional implications of the local E/I balance found experimentally (Figure 5), we modeled in detail the ten L2/3 PNs reconstructed with E and I synapses shown in Figures S4 and S5. Passive and active membrane properties of these neurons were based on previously published biological values (see STAR Methods). E and I synapses were placed at the experimentally measured dendritic location and activated as described in STAR Methods, such that the firing rate of the modeled neurons matched the rates measured *in vivo* (O'Connor et al., 2010). These models, of which two are shown in Figures 6A and 6B, also replicated several active and passive dendritic properties observed in L2/3 PNs, including somatic spiking activity (red and blue traces in Figures 6A and 6B), backpropagating action potentials, the somatic input resistance, and membrane time constants (Figures 6C–6F). To mimic *in vivo* observed input distributions to L2/3 PNs, we incorporated oscillatory excitatory "sensory" inputs as well as background excitatory inputs. We also incorporated background inhibition as well as feedforward and feedback inhibition, each targeting specific dendritic domains corresponding to parvalbumin-expressing basket interneurons and somatostatin-expressing dendritic-targeting Martinotti interneurons, respectively (see STAR Methods).

As found experimentally (O'Connor et al., 2010), our L2/3 PN models produced a range of firing rates ranging from 0 Hz to 10 Hz, with example neurons firing 3 Hz (blue circles in Figures 6G–6J) and 10 Hz (red circles in Figures 6G–6J). This variance in somatic firing rate persisted despite the fact that all models have the same specific passive and active properties and the same E and I input frequencies. We found that the global E/I balance per PN (Figure 6G) was a strong indicator of the output firing rate (Figure 7F). Additionally, the somatic firing rate was correlated with the size of the neuron: the larger the surface area of the neuron, the lower is its firing rate (Figure 6H). Although the larger surface area means lower input resistance that raises the threshold for action potentials, this higher threshold does not explain the inverse relationship between size and firing rate, as larger neurons also have more synapses that compensate for the lower input resistance (Figure 6I). The inverse relationship between size and firing rate might be due to the fact that neurons with larger surface area also tend to have a lower global E/I ratio (Figure 6J).

To test the significance of the local branch-specific E-to-I correlation found experimentally (Figure 5), we changed the

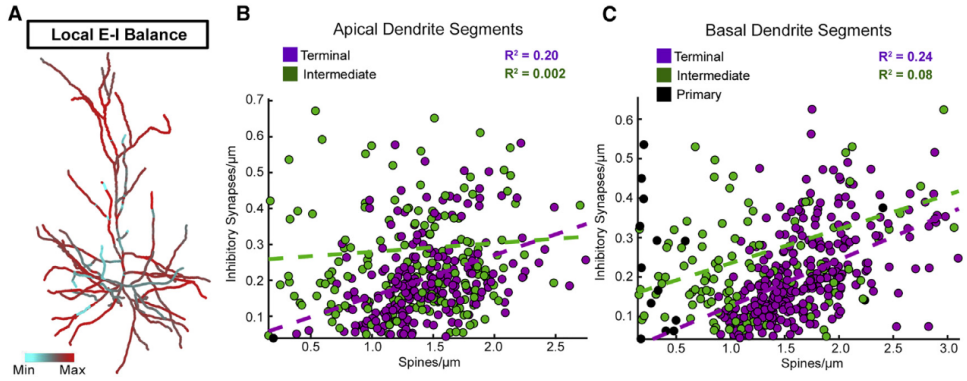


**Figure 5. Local E/I Balance within Branch Types**

(A) Heatmap of local E/I balance. Densities of E and I synapses were normalized to 1, and the absolute value of their difference is mapped within an adaptive range of each point across the dendritic tree (see STAR Methods). Values close to 0 therefore represent points on the dendritic tree at which the relative densities of E and I synapses were close to equivalent (Max), and values close to 1 represent points at which the relative densities of E and I synapses were much different from one another (Min).

(B) Relation between E and I synaptic density for intermediate (green; $R^2 = 0.002$; $p > 0.05$) and terminal (purple; $R^2 = 0.20$; $p < 6.6e^{-13}$) apical dendritic segments.

(C) Relation between E and I synaptic density for primary (black), intermediate (green; $R^2 = 0.08$; $p < 0.0007$) and terminal (purple; $R^2 = 0.24$; $p < 5.3e^{-19}$) basal dendritic segments.

STAR Methods

variance of the E/I ratio over all branches belonging to a specific domain while keeping the total number of synapses within each domain constant (thus keeping the global E/I ratio fixed for the modeled neuron, see STAR Methods). This created a distribution of standard deviation (SD) values for the E/I ratios, ranging from very low SD value, in which each segment within a given domain had very similar E/I ratio (Figure 7A, the balanced case, left), to the extreme case of large SD value, in which each branch in a given domain had either only excitatory or only inhibitory synapses (Figure 7B, the unbalanced case, left). Manipulation of the variance of the segment-specific E/I ratio had a strong effect on dendritic voltage dynamics (Figures 7A and 7B, right). In balanced dendrites, the variability in dendritic voltage (including active dendritic spiking and backpropagating action potentials (STAR Methods; Figures 7A and 7B) is dampened and overall more hyperpolarized (Figure 7A, right) compared to the unbalanced case (Figure 7B, right). In the case of minimal SD in the E/I ratio, the voltage distribution was narrower and very similar to that predicted from the biologically observed E/I ratio (compare blue to green curves in Figure 7C). Notice that this effect, shown here in *in vivo*-like input conditions with shared oscillatory input, was even stronger in the case of random input with a constant rate (Figure S7A). Additionally, this effect remained present whether we assigned a constant conductance to each synaptic input or varied the conductance of each synaptic input to linearly correlate with its volume (Figures S7B and S7C). We found that terminal domains, which experimentally had a near-balanced E/I ratio (Figure 5), were highly sensitive to the increase in the SD of the E/I ratio. Increasing SD gradually among dendritic segments resulted in a gradual increase of the mean dendritic voltage time-integral (Figure 7D). This was not the case for intermediate domains with a biologically unbalanced E/I ratio, where the change in the SD of the E/I ratio between segments had a minimal effect on the dendritic voltage time-integral (Figure 7G; see STAR Methods). This is likely due to the small contribution of intermediate synapses to the voltage perturbations in those domains, possibly as a result of their small relative number. Indeed, when performing the simulations after removing the synapses in intermediate domains, the voltage integral was reduced by less than 1% compared to 10%–30% when removing the synapses in the terminal domains (Figure S7A).

The somatic firing rate in the ten modeled neurons was also strongly affected by the domain-specific E/I SD value (keeping the global E/I balance fixed per neuron). Indeed, when testing the combined effect of differences in the global E/I ratio for different modeled neurons together with the effect of the domain-specific E/I SD, we found a high correlation ($R^2 = 0.74$ dashed line) between the somatic firing rate and the global E/I ratio (Figure 7F). As expected, neurons with a larger relative number of excitatory synapses fired at higher rates. Surprisingly, in all modeled neurons, the output firing rate increased as much as 2-fold per neuron when the domain-specific SD of the E/I ratio was increased, suggesting that the local E/I ratio (on top of the global E/I ratio) must be considered for understanding how synaptic activity shapes the neuron's output. Indeed, our simulations show that a neuron with a relatively small global E/I ratio may increase its firing rate to be as high as a neuron with twice the global E/I ratio, solely by increasing the variance of local E/I ratios among basal terminal branches (Figure 7F). Our experimentally based modeling demonstrates that, in L2/3 PNs, domain-specific local E/I balance at the level of dendritic segments constrains dendritic voltage fluctuations and controls the firing rate of these neurons to a significant extent (Figures 7F and S6).

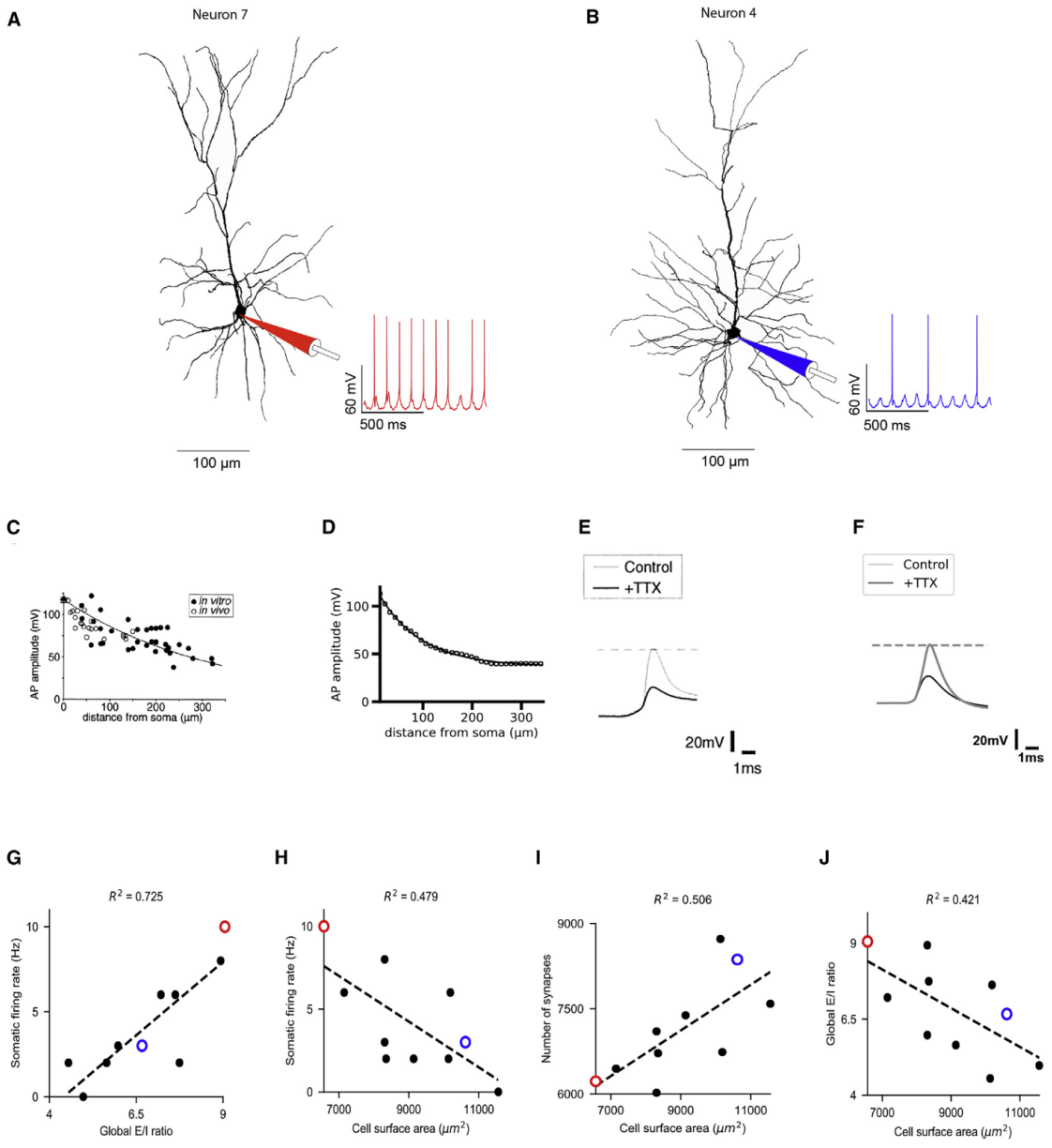


**Figure 6. Models Predict Large Variability in the Firing Rate of L2/3 PNs**

(A) The reconstructed morphology of neuron #7. Excitatory synapses were placed on the experimentally measured locations of the respective dendritic spines (5,604 E synapses in total); inhibitory synapses (619 in total) were placed at their experimentally measured location. The E and I synapses were activated as described in STAR Methods. Simulated membrane voltage was recorded from modeled soma (trace at bottom right).

(B) As in (A), with the morphology and traces belonging to neuron #4 (5,661 excitatory synapses and 785 inhibitory synapses).

(C) Backpropagating action potentials (BPAPs) in L2/3 PNs attenuate along the apical trunk (taken from the experiments in Waters et al., 2003). The y axis shows the amplitude of the BPAPs as a function of distances from the soma along the apical trunk: both *in vivo* (empty dots) and *in vitro* (solid dots) cases are shown.

(D) Same as in (C), in the simulated model of neuron #2.

(E) Action potential amplitude recorded 80 µm from the soma in the apical trunk with and without TTX (from Waters et al., 2003).

(F) Same as in (E), in model neuron #2.

*(legend continued on next page)*

## DISCUSSION

Mapping the spatial features of synaptic organization across whole neurons is crucial for bridging the gap between our understanding of the molecular determinants of synaptic development and the principles of circuit connectivity and function. Here, we developed an adaptable open-source toolkit for mapping the morphology and spatial distribution of all E and I synapses across complete neurons. This method has several key benefits for mapping subcellular synaptic morphology and distribution. As part of the Vaa3D image annotation platform, Synapse Detector is fully integrated into the Vaa3D automatic pipeline for image segmentation, 3D image stitching, and surface reconstruction (Chen et al., 2017; Peng et al., 2014, 2010). Synapse Detector is compatible with any fluorescent imaging method, including high resolution confocal microscopy. Synapse Detector provides a generalizable toolkit for quantifying and mapping features of subcellular fluorescent marker distribution. This flexibility allows these tools to probe the incredible diversity of synaptic compartments targeted to both dendritic spines and branches through structural mapping and computational modeling.

The synaptic mapping pipeline developed here enabled the reconstruction of twelve L2/3 PNs, including the location and morphology of over 90,000 E and I synapses. Previous anatomical studies of the synaptic morphology and connectivity of this neuron type allowed validation of our platform and observed results (Ballesteros-Yáñez et al., 2006; DeNardo et al., 2015; Frangeul et al., 2016; Kubota et al., 2007; Lefort et al., 2009; O'Connor et al., 2010). Our 3D reconstruction method for dendritic spines closely matched estimates from manual reconstructions of L2/3 PN spine density and morphology generated by tracing synapses from serial focal planes (Ballesteros-Yáñez et al., 2006). The fact that both E and I synaptic volumes appear to conform to log-normal distributions suggests that the cellular and molecular mechanisms underlying E and I synaptic size (most likely structural forms of synaptic plasticity) are multiplicative in nature rather than additive.

We also observed inhibitory synaptic distributions consistent with previous observations as well as a common proportion of inhibitory synapses targeted to spines in these mouse L2/3 PNs (Chen et al., 2012; Fossati et al., 2016; van Versendaal et al., 2012). Strikingly, the distribution of specific synaptic features characterizing these neurons recapitulates known motifs of circuit connectivity: in L2/3 PNs, dually innervated spines almost exclusively correspond to dendritic spines receiving thalamic inputs, and these synapses were significantly enriched in the L1 apical tufts and deep L3 basal dendrites, the two layers targeted by thalamic afferents from POm and VPM that innervate S1 (DeNardo et al., 2015; Kubota et al., 2007).

One limitation of our approach to label inhibitory synapses using expression of Gephyrin-EGFP expression is that, although it faithfully labels postsynaptic inhibitory synapses throughout the dendritic arbor of L2/3 PNs (Chen et al., 2012), this reporter tends to aggregate within the somas of these neurons, precluding labeling of peri-somatic inhibitory boutons made primarily by parvalbumin (PV)+ interneurons (large basket cells). This is the main reason why, in the present study, we focused our attention on the role of dendrite-targeting inhibitory synapses and their organization relative to excitatory synapses throughout the dendritic arbor of L2/3 PNs.

Analyzing the distribution of E and I synapses across complete dendritic arbors has revealed several scales of structured organization within L2/3 PNs. E and I synaptic distribution also varies significantly across dendritic domains, with fewer spines located in proximal than along distal dendritic segments.This organization, which is similar to patterns of synaptic distribution observed in CA1 PNs, potentially suggesting a shared principle for synaptic organization between these PN subtypes (Bloss et al., 2016; Megías et al., 2001).

Crucially, within-neuron comparisons of observed and randomized synaptic locations enabled the identification of structured distribution of E and I synapses to a restricted subset of dendritic segments within each domain. The formation of hotspots of synaptic density is consistent with known cellular mechanisms promoting spatially clustered synaptic stabilization and potentiation at the scale of single dendritic segments (Govindarajan et al., 2011; Losonczy et al., 2008). Active properties of dendrites critical for initiating clustered potentiation are engaged in somatosensory and visual cortical PNs during sensory processing, raising the tantalizing possibility that these hotspots of synaptic density might represent a structural signature of salient feature storage within neuronal dendrites (Frank et al., 2018; Smith et al., 2013; Takahashi et al., 2016; Xu et al., 2012).

A novel feature of structured synaptic distribution that emerged from our study is the strong, branch-specific, and local balance between E and I synaptic density across terminal dendritic segments. This suggests a far stronger association between E and I synaptic distribution than previous observations *in vitro* (Liu, 2004). Indeed, our data strongly suggest that molecular mechanisms co-regulating the balance between E and I synaptic density must be acting locally, at the scale of short dendritic segments. This spatial pattern closely matches the dendritic targeting of somatostatin-expressing interneurons, whose synapses onto L2/3 PNs were recently demonstrated to undergo NMDA receptor-dependent long-term potentiation (Chiu et al., 2018; Somogyi et al., 1998; Wang et al., 2004). While the study of E/I balance at the level of single neurons has largely been restricted to feedforward inhibition mediated by perisomatic-targeting basket interneurons, our whole-neuron synaptic input maps suggest that a precise balance between excitation and inhibition is critical for dendritic integration as well (Froemke, 2015; Xue et al., 2014).

(G) Correlation between somatic firing rate and the global E/I ratio for all 10 modeled neurons (filled circles). The Pearson coefficient is shown above the graph. Red and blue dots correspond to neurons #7 and #4 shown in (A) and (B), respectively.
(H) Same as in (G), with the x axis showing the neuron's surface area.
(I) Total number of synapses as a function of the total dendritic surface area.
(J) Global E/I ratio measured experimentally as a function of the total dendritic surface area.

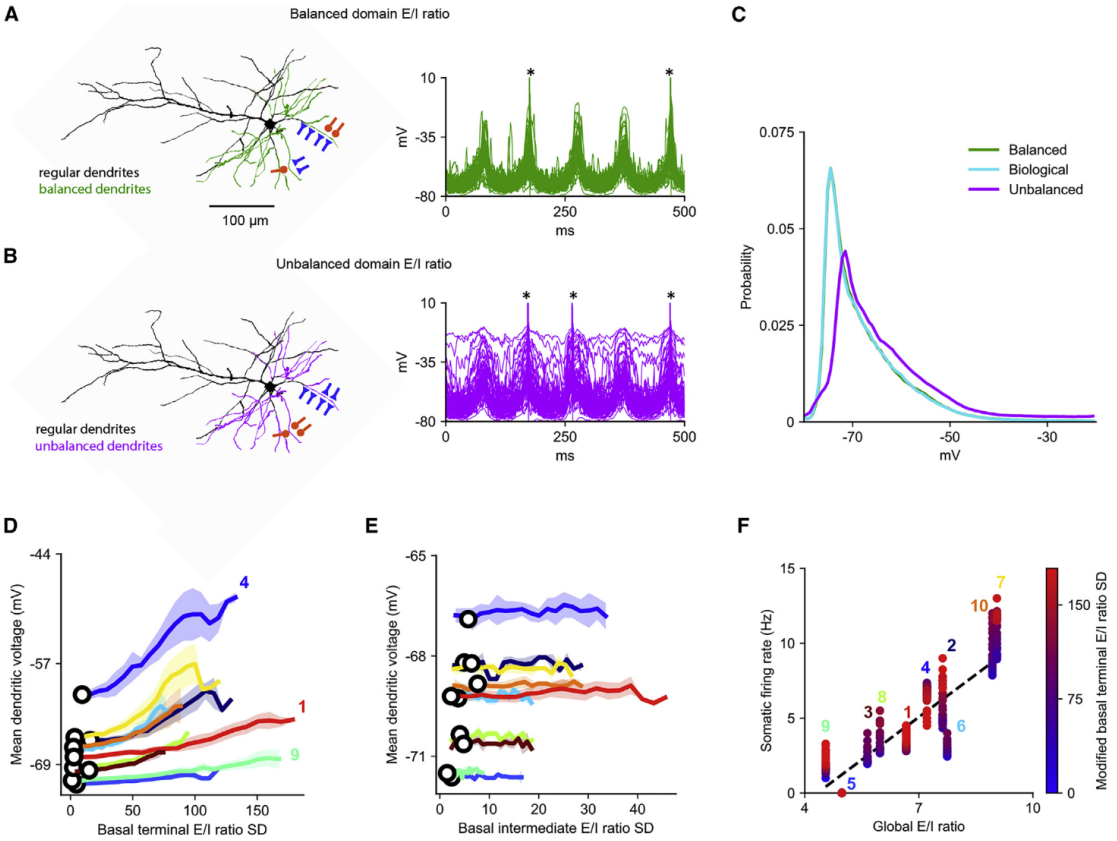


**Figure 7. Domain-Specific E/I Balance within L2/3 PNs Dampens Local Dendritic Voltage Fluctuations, Strongly Affecting the Global Output Firing Rate**

(A) Left: modeled L2/3 neuron (#2) in the case in which the E/I ratio is constant for all branches belonging to the distal apical domain (zero E/I SD, the balanced case). Right: voltage traces in all distal apical branches for the modeled neuron shown at left following synaptic activation (green traces). In this simulation, the E synapses (6,274 in total) and I synapses (1,111 in total) were distributed in a balanced fashion (schematically shown at left). Backpropagating action potentials are marked by an asterisk.

(B) Same as in (A) for the case of maximal E/I SD (the unbalanced case). In both (A) and (B), the total number of E and I synapses in the distal apical domain is fixed as found experimentally (same global balance for the two cases). Note that backpropagating action potentials (large depolarizing transient) exhibit higher frequencies in the unbalanced case.

(C) The probability of voltage integral for all branches in the basal terminal domain of the modeled neuron. The distribution of the dendritic voltage time-integral expected for the experimentally measured case (blue line) closely fits that expected in the balanced case (green line): both are narrower and less depolarized compared to that obtained in the unbalanced case (purple line).

(D) The average voltage time-integral for all segments in the basal terminal domain as a function of E/I SD in this domain (see STAR Methods). The open circles represent the biologically measured E/I SD values for each neuron. Numbers correspond to neuron numbers in Figure S4.

(E) As in (D) for the basal intermediate segments.

(F) Correlation between the somatic firing rate and the global E/I ratio for the 10 modeled neurons. In each neuron (numbered vertical lines), the domain-specific E/I SD was varied from the fully balanced case (blue) to the maximally unbalanced case (red). Numbers at each vertical line correspond to the modeled neuron identity. In all cases, the numbers of E and I synapses were taken from the experimental counts. Details of synaptic activation are described in STAR Methods.

The novel principle of synaptic organization uncovered in our study, whereby E and I synapses are locally balanced within dendritic branches, has significant implications for our understanding of the rules governing dendritic integration. Indeed, our modeling approach reveals that disrupting the biologically observed local dendritic E/I balance in terminal dendrites dramatically enhances local dendritic voltage fluctuations and the initiation of local dendritic non-linearities, resulting in increased firing at the soma. Importantly, our computational modeling of the spatially variable E/I ratio recapitulates both the subcellular targeting patterns and microcircuit properties of defined presynaptic neuronal subtypes, creating crucial context for the activation of synaptic inputs in their biologically observed dendritic distribution. Our first-ever complete mapping of E and I

synapses over the whole dendritic tree of a subtype of PNs, combined with detailed computational simulations, reveals that the spatially precise balance of E and I synapses we observed strongly impacts local dendritic computation as well as the global input-output dynamics of cortical neurons receiving synaptic inputs from the respective network. Finally, we provide here the open-source synaptic reconstruction tools we have developed as well as our complete dataset of 12 PN input maps containing information about the size, shape, and placement of over 90,000 E and I synapses.

## STAR★METHODS

Detailed methods are provided in the online version of this paper and include the following:

- KEY RESOURCES TABLE
- LEAD CONTACT AND MATERIALS AVAILABILITY
- EXPERIMENTAL MODEL AND SUBJECT DETAILS
  - Mice
- METHOD DETAILS
  - Constructs
  - In utero electroporation
  - Tissue preparation
  - Confocal imaging
- QUANTIFICATION AND STATISTICAL ANALYSIS
  - Software development
  - Neuron reconstruction
  - Automatic spine detection
  - Voxel clustering for enhanced detection
  - Intensity-based segmentation of adjacent spines
  - Inhibitory synapse detection
  - Stitching neuron traces across serial 3D image sections
  - Neurite subtyping
  - User's guide
  - Synaptic map visualization
  - Synaptic distribution analysis
  - Modeling
- DATA AND CODE AVAILABILITY

## SUPPLEMENTAL INFORMATION

Supplemental Information can be found online at https://doi.org/10.1016/j.neuron.2020.02.015.

## ACKNOWLEDGMENTS

We thank Attila Losonczy, Wes Grueber, Inbal Israeli, and members of the Polleux lab for fruitful discussions. This work was supported by grants from the NIH (RO1 NS067557 to F.P., F31 NS101820 to D.M.I., and R21 NS109753 to H.B.); an award from the Roger De Spoelberch foundation (to F.P.); the NSF (1564736 to Y.L. and NeuroNex Award DBI-1707398 to L.F.A.); ARO MURI (W911NF-12-1-0594 to U.S.); DoI/IBC IARPA (D16PC00008 to U.S.); the Gatsby Charitable Foundation (to L.F.A. and I.S.); and the Human Brain Project (grant agreement no. 604102 to I.S.).

## AUTHOR CONTRIBUTIONS

D.M.I. and F.P. designed the study. D.M.I. developed the labeling and imaging protocol and performed cloning, animal surgery, and imaging. Y.L. and H.P. developed the Synapse Detector and Subtree Labeling programs with assistance from D.M.I. for user interface design. U.S. developed the anatomical synaptic distribution analysis with assistance from D.M.I. and generated neuron heatmaps. M.D. and I.S. performed computational modeling experiments in coordination with D.M.I. Y.L. and H.C. developed the trace stitching program. D.M.I., V.A., and F.G. generated neuron reconstructions using Synapse Detector. H.B. performed animal surgery. L.F.A. performed the synaptic morphology analysis. D.M.I., Y.L., U.S., M.D., I.S., H.P., and F.P. wrote the paper.

## DECLARATION OF INTERESTS

The authors declare no competing interests.

Received: November 5, 2018
Revised: April 19, 2019
Accepted: February 11, 2020
Published: March 12, 2020

## REFERENCES

Acciai, L., Soda, P., and Iannello, G. (2016). Automated Neuron Tracing Methods: An Updated Account. Neuroinformatics *14*, 353–367.

Alonso-Nanclares, L., White, E.L., Elston, G.N., and DeFelipe, J. (2004). Synaptology of the proximal segment of pyramidal cell basal dendrites. Eur. J. Neurosci. *19*, 771–776.

Arellano, J.I., Benavides-Piccione, R., Defelipe, J., and Yuste, R. (2007). Ultrastructure of dendritic spines: correlation between synaptic and spine morphologies. Front. Neurosci. *1*, 131–143.

Ascoli, G.A. (2006). Mobilizing the base of neuroscience data: the case of neuronal morphologies. Nat. Rev. Neurosci. *7*, 318–324.

Atasoy, D., Aponte, Y., Su, H.H., and Sternson, S.M. (2008). A FLEX switch targets Channelrhodopsin-2 to multiple cell types for imaging and long-range circuit mapping. J. Neurosci. *28*, 7025–7030.

Ballesteros-Yáñez, I., Benavides-Piccione, R., Elston, G.N., Yuste, R., and DeFelipe, J. (2006). Density and morphology of dendritic spines in mouse neocortex. Neuroscience *138*, 403–409.

Barnes, R., Lehman, C., and Mulla, D. (2014). Priority-Flood: An Optimal Depression-Filling and Watershed-Labeling Algorithm for Digital Elevation Models. Computers & Geosciences *62*, 117–127.

Bloss, E.B., Cembrowski, M.S., Karsh, B., Colonell, J., Fetter, R.D., and Spruston, N. (2016). Structured Dendritic Inhibition Supports Branch-Selective Integration in CA1 Pyramidal Cells. Neuron *89*, 1016–1030.

Bourne, J.N., and Harris, K.M. (2011). Coordination of size and number of excitatory and inhibitory synapses results in a balanced structural plasticity along mature hippocampal CA1 dendrites during LTP. Hippocampus *21*, 354–373.

Carnevale, N.T., and Hines, M.L. (2006). The NEURON Book (Cambridge University Press).

Charrier, C., Joshi, K., Coutinho-Budd, J., Kim, J.E., Lambert, N., de Marchena, J., Jin, W.L., Vanderhaeghen, P., Ghosh, A., Sassa, T., and Polleux, F. (2012). Inhibition of SRGAP2 function by its human-specific paralogs induces neoteny during spine maturation. Cell *149*, 923–935.

Chen, J.L., Villa, K.L., Cha, J.W., So, P.T., Kubota, Y., and Nedivi, E. (2012). Clustered dynamics of inhibitory synapses and dendritic spines in the adult neocortex. Neuron *74*, 361–373.

Chen, H., Iascone, D.M., da Costa, N.M., Lein, E.S., Liu, T., and Peng, H. (2017). Fast assembling of neuron fragments in serial 3D sections. Brain Inform. *4*, 183–186.

Chiu, C.Q., Lur, G., Morse, T.M., Carnevale, N.T., Ellis-Davies, G.C., and Higley, M.J. (2013). Compartmentalization of GABAergic inhibition by dendritic spines. Science *340*, 759–762.

Chiu, C.Q., Martenson, J.S., Yamazaki, M., Natsume, R., Sakimura, K., Tomita, S., Tavalin, S.J., and Higley, M.J. (2018). Input-Specific NMDAR-Dependent Potentiation of Dendritic GABAergic Inhibition. Neuron *97*, 368–377.e363.

Conchello, J.A., and Lichtman, J.W. (2005). Optical sectioning microscopy. Nat. Methods *2*, 920–931.

D'amour, J.A., and Froemke, R.C. (2015). Inhibitory and excitatory spike-timing-dependent plasticity in the auditory cortex. Neuron *86*, 514–528.

de Vivo, L., Bellesi, M., Marshall, W., Bushong, E.A., Ellisman, M.H., Tononi, G., and Cirelli, C. (2017). Ultrastructural evidence for synaptic scaling across the wake/sleep cycle. Science *355*, 507–510.

DeFelipe, J., Alonso-Nanclares, L., and Arellano, J.I. (2002). Microstructure of the neocortex: comparative aspects. J. Neurocytol. *31*, 299–316.

DeNardo, L.A., Berns, D.S., DeLoach, K., and Luo, L. (2015). Connectivity of mouse somatosensory and prefrontal cortex examined with trans-synaptic tracing. Nat. Neurosci. *18*, 1687–1697.

Dickstein, D.L., Dickstein, D.R., Janssen, W.G., Hof, P.R., Glaser, J.R., Rodriguez, A., O'Connor, N., Angstman, P., and Tappan, S.J. (2016). Automatic Dendritic Spine Quantification from Confocal Data with Neurolucida 360. Curr Protoc Neurosci. *77*, 1.27.1–1.27.21.

Dorrn, A.L., Yuan, K., Barker, A.J., Schreiner, C.E., and Froemke, R.C. (2010). Developmental sensory experience balances cortical excitation and inhibition. Nature *465*, 932–936.

Feldmeyer, D. (2012). Excitatory neuronal connectivity in the barrel cortex. Front. Neuroanat. *6*, 24.

Feldmeyer, D., Lübke, J., Silver, R.A., and Sakmann, B. (2002). Synaptic connections between layer 4 spiny neurone-layer 2/3 pyramidal cell pairs in juvenile rat barrel cortex: physiology and anatomy of interlaminar signalling within a cortical column. J. Physiol. *538*, 803–822.

Fogarty, M.J., Hammond, L.A., Kanjhan, R., Bellingham, M.C., and Noakes, P.G. (2013). A method for the three-dimensional reconstruction of Neurobiotin™-filled neurons and the location of their synaptic inputs. Front. Neural Circuits *7*, 153.

Fossati, M., Pizzarelli, R., Schmidt, E.R., Kupferman, J.V., Stroebel, D., Polleux, F., and Charrier, C. (2016). SRGAP2 and Its Human-Specific Paralog Co-Regulate the Development of Excitatory and Inhibitory Synapses. Neuron *91*, 356–369.

Frangeul, L., Pouchelon, G., Telley, L., Lefort, S., Luscher, C., and Jabaudon, D. (2016). A cross-modal genetic framework for the development and plasticity of sensory pathways. Nature *538*, 96–98.

Frank, A.C., Huang, S., Zhou, M., Gdalyahu, A., Kastellakis, G., Silva, T.K., Lu, E., Wen, X., Poirazi, P., Trachtenberg, J.T., and Silva, A.J. (2018). Hotspots of dendritic spine turnover facilitate clustered spine addition and learning and memory. Nat. Commun. *9*, 422.

Froemke, R.C. (2015). Plasticity of cortical excitatory-inhibitory balance. Annu. Rev. Neurosci. *38*, 195–219.

Gidon, A., and Segev, I. (2012). Principles governing the operation of synaptic inhibition in dendrites. Neuron *75*, 330–341.

Govindarajan, A., Israely, I., Huang, S.Y., and Tonegawa, S. (2011). The dendritic branch is the preferred integrative unit for protein synthesis-dependent LTP. Neuron *69*, 132–146.

Haider, B., and McCormick, D.A. (2009). Rapid neocortical dynamics: cellular and network mechanisms. Neuron *62*, 171–189.

Halavi, M., Hamilton, K.A., Parekh, R., and Ascoli, G.A. (2012). Digital reconstructions of neuronal morphology: three decades of research trends. Front. Neurosci. *6*, 49.

Hand, R., and Polleux, F. (2011). Neurogenin2 regulates the initial axon guidance of cortical pyramidal neurons projecting medially to the corpus callosum. Neural Dev. *6*, 30.

Harris, K.M., and Kater, S.B. (1994). Dendritic spines: cellular specializations imparting both stability and flexibility to synaptic function. Annu. Rev. Neurosci. *17*, 341–371.

Harvey, C.D., and Svoboda, K. (2007). Locally dynamic synaptic learning rules in pyramidal neuron dendrites. Nature *450*, 1195–1200.

Hayashi, M.K., Tang, C., Verpelli, C., Narayanan, R., Stearns, M.H., Xu, R.M., Li, H., Sala, C., and Hayashi, Y. (2009). The postsynaptic density proteins Homer and Shank form a polymeric network structure. Cell *137*, 159–171.

Helmstaedter, M. (2013). Cellular-resolution connectomics: challenges of dense neural circuit reconstruction. Nat. Methods *10*, 501–507.

Helmstaedter, M., Briggman, K.L., and Denk, W. (2008). 3D structural imaging of the brain with photons and electrons. Curr. Opin. Neurobiol. *18*, 633–641.

Higley, M.J., and Contreras, D. (2006). Balanced excitation and inhibition determine spike timing during frequency adaptation. J. Neurosci. *26*, 448–457.

Hildebrand, D.G.C., Cicconet, M., Torres, R.M., Choi, W., Quan, T.M., Moon, J., Wetzel, A.W., Scott Champion, A., Graham, B.J., Randlett, O., et al. (2017). Whole-brain serial-section electron microscopy in larval zebrafish. Nature *545*, 345–349.

Iacaruso, M.F., Gasler, I.T., and Hofer, S.B. (2017). Synaptic organization of visual space in primary visual cortex. Nature *547*, 449–452.

Isaacson, J.S., and Scanziani, M. (2011). How inhibition shapes cortical activity. Neuron *72*, 231–243.

Jiang, X., Shen, S., Cadwell, C.R., Berens, P., Sinz, F., Ecker, A.S., Patel, S., and Tolias, A.S. (2015). Principles of connectivity among morphologically defined cell types in adult neocortex. Science *350*, aac9462.

Kasugai, Y., Swinny, J.D., Roberts, J.D., Dalezios, Y., Fukazawa, Y., Sieghart, W., Shigemoto, R., and Somogyi, P. (2010). Quantitative localisation of synaptic and extrasynaptic GABAA receptor subunits on hippocampal pyramidal cells by freeze-fracture replica immunolabelling. Eur. J. Neurosci. *32*, 1868–1888.

Katz, Y., Menon, V., Nicholson, D.A., Geinisman, Y., Kath, W.L., and Spruston, N. (2009). Synapse distribution suggests a two-stage model of dendritic integration in CA1 pyramidal neurons. Neuron *63*, 171–177.

Kleindienst, T., Winnubst, J., Roth-Alpermann, C., Bonhoeffer, T., and Lohmann, C. (2011). Activity-dependent clustering of functional synaptic inputs on developing hippocampal dendrites. Neuron *72*, 1012–1024.

Kleinfeld, D., Bharioke, A., Blinder, P., Bock, D.D., Briggman, K.L., Chklovskii, D.B., Denk, W., Helmstaedter, M., Kaufhold, J.P., Lee, W.C., et al. (2011). Large-scale automated histology in the pursuit of connectomes. J. Neurosci. *31*, 16125–16138.

Knott, G.W., Holtmaat, A., Wilbrecht, L., Welker, E., and Svoboda, K. (2006). Spine growth precedes synapse formation in the adult neocortex in vivo. Nat. Neurosci. *9*, 1117–1124.

Kubota, Y., Hatada, S., Kondo, S., Karube, F., and Kawaguchi, Y. (2007). Neocortical inhibitory terminals innervate dendritic spines targeted by thalamocortical afferents. J. Neurosci. *27*, 1139–1150.

Lefort, S., Tomm, C., Floyd Sarria, J.C., and Petersen, C.C. (2009). The excitatory neuronal network of the C2 barrel column in mouse primary somatosensory cortex. Neuron *61*, 301–316.

Liu, G. (2004). Local structural balance and functional interaction of excitatory and inhibitory synapses in hippocampal dendrites. Nat. Neurosci. *7*, 373–379.

Losonczy, A., Makara, J.K., and Magee, J.C. (2008). Compartmentalized dendritic plasticity and input feature storage in neurons. Nature *452*, 436–441.

Lübke, J., Egger, V., Sakmann, B., and Feldmeyer, D. (2000). Columnar organization of dendrites and axons of single and synaptically coupled excitatory spiny neurons in layer 4 of the rat barrel cortex. J. Neurosci. *20*, 5300–5311.

Majewska, A., Tashiro, A., and Yuste, R. (2000). Regulation of spine calcium dynamics by rapid spine motility. J. Neurosci. *20*, 8262–8268.

Makino, H., and Malinow, R. (2011). Compartmentalized versus global synaptic plasticity on dendrites controlled by experience. Neuron *72*, 1001–1011.

Markram, H., Muller, E., Ramaswamy, S., Reimann, M.W., Abdellah, M., Sanchez, C.A., Ailamaki, A., Alonso-Nanclares, L., Antille, N., Arsever, S., et al. (2015). Reconstruction and Simulation of Neocortical Microcircuitry. Cell *163*, 456–492.

Marlin, B.J., Mitre, M., D'amour, J.A., Chao, M.V., and Froemke, R.C. (2015). Oxytocin enables maternal behaviour by balancing cortical inhibition. Nature *520*, 499–504.

Matsuzaki, M., Honkura, N., Ellis-Davies, G.C., and Kasai, H. (2004). Structural basis of long-term potentiation in single dendritic spines. Nature *429*, 761–766.

Megías, M., Emri, Z., Freund, T.F., and Gulyás, A.I. (2001). Total number and distribution of inhibitory and excitatory synapses on hippocampal CA1 pyramidal cells. Neuroscience *102*, 527–540.

Meijering, E. (2010). Neuron tracing in perspective. Cytometry A *77*, 693–704.

Meijering, E., Carpenter, A.E., Peng, H., Hamprecht, F.A., and Olivo-Marin, J.C. (2016). Imagining the future of bioimage analysis. Nat. Biotechnol. *34*, 1250–1255.

Mollenhauer, H.H. (1993). Artifacts caused by dehydration and epoxy embedding in transmission electron microscopy. Microsc. Res. Tech. *26*, 496–512.

Nimchinsky, E.A., Sabatini, B.L., and Svoboda, K. (2002). Structure and function of dendritic spines. Annu. Rev. Physiol. *64*, 313–353.

O'Connor, D.H., Peron, S.P., Huber, D., and Svoboda, K. (2010). Neural activity in barrel cortex underlying vibrissa-based object localization in mice. Neuron *67*, 1048–1061.

Peng, H., Ruan, Z., Long, F., Simpson, J.H., and Myers, E.W. (2010). V3D enables real-time 3D visualization and quantitative analysis of large-scale biological image data sets. Nat. Biotechnol. *28*, 348–353.

Peng, H., Long, F., and Myers, G. (2011). Automatic 3D neuron tracing using all-path pruning. Bioinformatics *27*, i239–i247.

Peng, H., Bria, A., Zhou, Z., Iannello, G., and Long, F. (2014). Extensible visualization and analysis for multidimensional images using Vaa3D. Nat. Protoc. *9*, 193–208.

Pennacchietti, F., Vascon, S., Nieus, T., Rosillo, C., Das, S., Tyagarajan, S.K., Diaspro, A., Del Bue, A., Petrini, E.M., Barberis, A., and Cella Zanacchi, F. (2017). Nanoscale Molecular Reorganization of the Inhibitory Postsynaptic Density Is a Determinant of GABAergic Synaptic Potentiation. J. Neurosci. *37*, 1747–1756.

Petreanu, L., Mao, T., Sternson, S.M., and Svoboda, K. (2009). The subcellular organization of neocortical excitatory connections. Nature *457*, 1142–1145.

Petrini, E.M., Ravasenga, T., Hausrat, T.J., Iurilli, G., Olcese, U., Racine, V., Sibarita, J.B., Jacob, T.C., Moss, S.J., Benfenati, F., et al. (2014). Synaptic recruitment of gephyrin regulates surface GABAA receptor dynamics for the expression of inhibitory LTP. Nat. Commun. *5*, 3921.

Polsky, A., Mel, B.W., and Schiller, J. (2004). Computational subunits in thin dendrites of pyramidal cells. Nat. Neurosci. *7*, 621–627.

Rodriguez, A., Ehlenberger, D.B., Dickstein, D.L., Hof, P.R., and Wearne, S.L. (2008). Automated three-dimensional detection and shape classification of dendritic spines from fluorescence microscopy images. PLoS ONE *3*, e1997.

Santuy, A., Rodríguez, J.R., DeFelipe, J., and Merchán-Pérez, A. (2018a). Study of the Size and Shape of Synapses in the Juvenile Rat Somatosensory Cortex with 3D Electron Microscopy. eNeuro *5*, 5.

Santuy, A., Rodriguez, J.R., DeFelipe, J., and Merchan-Perez, A. (2018b). Volume electron microscopy of the distribution of synapses in the neuropil of the juvenile rat somatosensory cortex. Brain Struct. Funct. *223*, 77–90.

Sarid, L., Bruno, R., Sakmann, B., Segev, I., and Feldmeyer, D. (2007). Modeling a layer 4-to-layer 2/3 module of a single column in rat neocortex: interweaving in vitro and in vivo experimental observations. Proc. Natl. Acad. Sci. USA *104*, 16353–16358.

Schikorski, T., and Stevens, C.F. (2001). Morphological correlates of functionally defined synaptic vesicle populations. Nat. Neurosci. *4*, 391–395.

Schnütgen, F., Doerflinger, N., Calléja, C., Wendling, O., Chambon, P., and Ghyselinck, N.B. (2003). A directional strategy for monitoring Cre-mediated recombination at the cellular level in the mouse. Nat. Biotechnol. *21*, 562–565.

Sigal, Y.M., Speer, C.M., Babcock, H.P., and Zhuang, X. (2015). Mapping Synaptic Input Fields of Neurons with Super-Resolution Imaging. Cell *163*, 493–505.

Smith, S.L., Smith, I.T., Branco, T., and Häusser, M. (2013). Dendritic spikes enhance stimulus selectivity in cortical neurons in vivo. Nature *503*, 115–120.

Somogyi, P., Tamás, G., Lujan, R., and Buhl, E.H. (1998). Salient features of synaptic organisation in the cerebral cortex. Brain Res. Brain Res. Rev. *26*, 113–135.

Spacek, J., and Hartmann, M. (1983). Three-dimensional analysis of dendritic spines. I. Quantitative observations related to dendritic spine and synaptic morphology in cerebral and cerebellar cortices. Anat. Embryol. (Berl.) *167*, 289–310.

Spruston, N. (2008). Pyramidal neurons: dendritic structure and synaptic integration. Nat. Rev. Neurosci. *9*, 206–221.

Takahashi, N., Oertner, T.G., Hegemann, P., and Larkum, M.E. (2016). Active cortical dendrites modulate perception. Science *354*, 1587–1590.

Tremblay, R., Lee, S., and Rudy, B. (2016). GABAergic Interneurons in the Neocortex: From Cellular Properties to Circuits. Neuron *91*, 260–292.

Usui, S., Konno, D., Hori, K., Maruoka, H., Okabe, S., Fujikado, T., Tano, Y., and Sobue, K. (2003). Synaptic targeting of PSD-Zip45 (Homer 1c) and its involvement in the synaptic accumulation of F-actin. J. Biol. Chem. *278*, 10619–10628.

van Versendaal, D., Rajendran, R., Saiepour, M.H., Klooster, J., Smit-Rigter, L., Sommeijer, J.P., De Zeeuw, C.I., Hofer, S.B., Heimel, J.A., and Levelt, C.N. (2012). Elimination of inhibitory synapses is a major component of adult ocular dominance plasticity. Neuron *74*, 374–383.

Vetter, P., Roth, A., and Häusser, M. (2001). Propagation of action potentials in dendrites depends on dendritic morphology. J. Neurophysiol. *85*, 926–937.

Wang, Y., Toledo-Rodriguez, M., Gupta, A., Wu, C., Silberberg, G., Luo, J., and Markram, H. (2004). Anatomical, physiological and molecular properties of Martinotti cells in the somatosensory cortex of the juvenile rat. J. Physiol. *561*, 65–90.

Waters, J., Larkum, M., Sakmann, B., and Helmchen, F. (2003). Supralinear Ca2+ influx into dendritic tufts of layer 2/3 neocortical pyramidal neurons in vitro and in vivo. J. Neurosci. *23*, 8558–8567.

Xu, N.L., Harnett, M.T., Williams, S.R., Huber, D., O'Connor, D.H., Svoboda, K., and Magee, J.C. (2012). Nonlinear dendritic integration of sensory and motor input during an active sensing task. Nature *492*, 247–251.

Xue, M., Atallah, B.V., and Scanziani, M. (2014). Equalizing excitation-inhibition ratios across visual cortical neurons. Nature *511*, 596–600.

## STAR★METHODS

### KEY RESOURCES TABLE

| REAGENT or RESOURCE | SOURCE | IDENTIFIER |
|---|---|---|
| Critical Commercial Assays | | |
| In-Fusion HD cloning kit | Clontech | 639649 |
| Deposited Data | | |
| P42 CD-1 IGS mouse L2/3 S1 neuron 1 (E and I) | This Paper | N/A |
| P42 CD-1 IGS mouse L2/3 S1 neuron 2 (E and I) | This Paper | N/A |
| P42 CD-1 IGS mouse L2/3 S1 neuron 3 (E and I) | This Paper | N/A |
| P42 CD-1 IGS mouse L2/3 S1 neuron 4 (E and I) | This Paper | N/A |
| P42 CD-1 IGS mouse L2/3 S1 neuron 5 (E and I) | This Paper | N/A |
| P42 CD-1 IGS mouse L2/3 S1 neuron 6 (E and I) | This Paper | N/A |
| P42 CD-1 IGS mouse L2/3 S1 neuron 7 (E and I) | This Paper | N/A |
| P42 CD-1 IGS mouse L2/3 S1 neuron 8 (E and I) | This Paper | N/A |
| P42 CD-1 IGS mouse L2/3 S1 neuron 9 (E and I) | This Paper | N/A |
| P42 CD-1 IGS mouse L2/3 S1 neuron 10 (E and I) | This Paper | N/A |
| P42 CD-1 IGS mouse L2/3 S1 neuron 11 (E only) | This Paper | N/A |
| P42 CD-1 IGS mouse L2/3 S1 neuron 12 (E only) | This Paper | N/A |
| Experimental Models: Organisms/Strains | | |
| Mouse: CD-1 IGS | Charles River | Cat# 022 |
| Recombinant DNA | | |
| Plasmid: pCAG NLS-Cre | This Paper | N/A |
| Plasmid: pCAG EGFP-GPHN | This Paper | N/A |
| Plasmid: pEf1α FLEX-tdTomato | This Paper | N/A |
| Software and Algorithms | | |
| Vaa3D | Peng et al., 2010 | http://home.penglab.com/proj/vaa3d/ |
| Spine Detector | This Paper | http://home.penglab.com/proj/vaa3d/ |
| IS Detector | This Paper | http://home.penglab.com/proj/vaa3d/ |
| Subtree Labeling | This Paper | http://home.penglab.com/proj/vaa3d/ |
| Neuron Stitcher | Chen et al., 2017 | http://home.penglab.com/proj/vaa3d/ |
| NEURON | Carnevale and Hines, 2006 | https://www.neuron.yale.edu/ |
| MATLAB | The MathWorks Inc. | https://ch.mathworks.com/products/matlab/ |
| GraphPad PRISM | GraphPad Software Inc. | https://www.graphpad.com/scientific-software/prism/ |
| Other | | |
| A1R confocal microscope | Nikon | https://www.microscope.healthcare.nikon.com/products/confocal-microscopes/a1hd25-a1rhd25 |

### LEAD CONTACT AND MATERIALS AVAILABILITY

Further information and requests for resources and reagents should be directed to and will be fulfilled by the Lead Contact, Franck Polleux (fp2304@columbia.edu). All unique/stable reagents generated in this study are available from the Lead Contact without restriction.

### EXPERIMENTAL MODEL AND SUBJECT DETAILS

#### Mice

All animals were handled according to protocols approved by the Institutional Animal Care and Use Committee at Columbia University, New York. Postnatal day 42 CD-1 IGS mice (strain code: 022; Charles River) were used for all experiments. Timed-pregnant fe-

male mice were maintained in a 12 hour light/dark cycle and obtained by overnight breeding with males of the same strain. For timed-pregnant mating, noon after mating is considered E0.5.

## METHOD DETAILS

### Constructs

The tdTomato reporter insert was subcloned into the pAAV-Ef1a-DIO eNpHR 3.0-EYFP plasmid (Addgene plasmid # 26966) between the AscI and NheI cloning sites. EGFP-GPHN (clone P1) was obtained from H. Cline (TSRI, La Jolla, USA) and subcloned into pCAG downstream of a CMV-enhancer/chicken-β-actin (CAG) promoter, by replacing EGFP between the XmaI and NotI cloning sites.

### In utero electroporation

In utero cortical electroporation was performed at E15.5 on timed pregnant CD1 females. The previously described protocol for in utero cortical electroporation (Hand and Polleux, 2011) was modified as follows. Endotoxin-free DNA was injected using a glass pipette into one ventricle of the mouse embryos. The volume of injected DNA was adjusted depending on the experiments. Electroporation was performed at E15.5 using a square wave electroporator (ECM 830, BTX) and gold paddles. The electroporation settings were: 5 pulses of 45V for 50 ms with 500 ms intervals. Plasmids were used at the following concentrations: Flex-tdTomato reporter plasmid: 1 μg/μl; EGFP-GPHN 0.5 μg/μl; NLS-Cre recombinase: 200 pg/μl.

### Tissue preparation

Animals at the indicated age were anaesthetized with isofluorane before intracardiac perfusion with PBS and 4% PFA (Electron Microscopy Sciences). 130 μm coronal brain sections were obtained using a vibrating microtome (Leica VT1200S). Sections were mounted on slides and briefly dehydrated at room temperature to reduce section thickness before being coverslipped in Fluoromount-G (SouthernBiotech).

### Confocal imaging

Confocal images of electroporated neurons in slices were acquired in 1024x1024 mode using an A1R laser scanning confocal microscope controlled by the Nikon software NIS-Elements (Nikon Corporation, Melville, NY). We used a 100X H-TIRF, NA 1.49 (Nikon) objective lens to acquire image volumes of neuron fragments. Z stacks of images were acquired with spacing of 100 nm. To counteract possible interference from light diffraction through the tissue, laser power was linearly increased as a function of depth within each tissue section to normalize the mean fluorescent intensity of pixels from image planes throughout the stack (Figures S2A and S2B). Dendritic spines and inhibitory synapses were quantified based on tdTomato fluorescence and EGFP-GPHN puncta fluorescence respectively. All quantifications were performed in L2/3 somatosensory cortex in sections of comparable rostro-caudal position.

## QUANTIFICATION AND STATISTICAL ANALYSIS

### Software development

#### *Computational pipeline overview*

Information for dendritic spine placement and morphology was acquired from large-volume high-resolution image stacks of thick brain tissue. There are two possible strategies for quantifying the spatial distribution of excitatory and inhibitory (E and I) synapses of an entire neuron:

1. Stitch image volumes together prior to analysis.
2. Analyze each image volume independently and align the spatial information recorded from each image to create a complete neuron representation.

The first strategy, which involves all the image stacks into a terabyte volume and then perform neuron tracing, synapse segmentation and spatial analysis globally on the combined volume. The downside of the approach is a big data problem of manipulating, storing and analyzing the giant volume. Additionally, this approach is computationally wasteful because only a fraction of the stitched volume contains relevant structure. To avoid this big data problem, we pursued the alternative strategy of performing dendrite tracing and synapse segmentation on each image stack individually and associating morphological information of each synapse to a specific node of the trace (thereby encoding the location of every synapse within the spatial context of the neuron). To create representations of complete neurons across serial vibratome sections, dendrite traces containing synaptic information were aligned and stitched together. In comparison with the terabyte combined volume generated by the first reconstruction strategy, the resulting reconstructions are 4-6 megabytes in size.

Our pipeline for whole-neuron synaptic reconstruction consists of two parts. In the first part, we extract E and I synaptic information for an individual image across a tissue section (Figure S1A). For each image stack, we trace the dendritic arbor of the neuron fragment using automatic tracing methods followed by manual corrections. Then both Spine Detector and IS Detector take the neuron skeleton

and the image stack as input to automatically isolate spines and inhibitory synapses within a user-defined radius of each dendrite. Spine Detector generates a table that records the local information of dendritic spines including the distance between each synapse and the dendrite, volume, and the nearest tree node. IS Detector generates a table that records the local information of inhibitory synapses including volume, whether the inhibitory synapse is located on a spine or the dendrite, and the nearest tree node. These morphological characteristics of synapses impact their neurotransmitter content and integration properties (Chiu et al., 2013; Kasugai et al., 2010; Majewska et al., 2000; Schikorski and Stevens, 2001).

In the second part of our reconstruction pipeline, we map E and I synaptic morphology across multiple images for whole-neuron spatial distribution analysis (Figure S1B). First, the dendritic spine information and inhibitory synaptic information from each image are mapped to the closest tree node of their corresponding dendrite trace. Next, the traces containing local synaptic information from each image stack are aligned and stitched together to generate a whole-neuron synaptic reconstruction. Notably, the association between synapses and their respective tree nodes remains unchanged during the assembly. After obtaining the single reconstruction trace of the whole neuron, we subtype the dendritic arbor in terms of identity and morphology so that we can analyze the synaptic features within domain and segment levels.

### Neuron reconstruction

Digital reconstructions, or traces, are an effective representation of neuronal topology and geometry. The traces are usually described using a tree graph and consist of 3-D point coordinates, diameters, and connectivity between points. This succinct representation enables an extensive quantitative analyses of the geometrical organization of the neurons they represent including total length, branching angles, distribution statistics and cumulative distance from the soma (Ascoli, 2006). Numerous automated tracing methods have been developed (Acciai et al., 2016; Halavi et al., 2012; Meijering, 2010). In this paper, the initial reconstructions are obtained using the automatic tracing methods built in the open source 3D visualization and analysis tool Vaa3D (Peng et al., 2014). Then, experts manually proofread the traces and make adjustments with the built-in proof-editing tools. Notably our synapse analysis pipeline works for traces generated by all tracing methods. Accurate reconstructions are important to improve the performance of automatic synapse detection.

### Automatic spine detection

To automatically identify potential spines, Spine Detector segments candidate spine-associated voxels whose fluorescence is greater than a linearly interpolated local threshold between nodes along the closest dendritic segment (Rodriguez et al., 2008). Spine detection is performed within a user-defined region around the dendrite and intensity threshold such that all voxels within the user-defined region and above the threshold are identified possible spine voxels. Spine Detector takes both the image and the dendritic trace as input and clusters adjacent voxels in the cell-fill channel based on their distance from the dendrite surface. Touching spines are separated based on voxel intensities. Because the dendrite traces represent the dendrites with a series of overlapping nodes (Peng et al., 2011), information about the volume and distance from the dendrite of each spine can be associated with its nearest node to assign a location within the spatial context of the dendritic arbor.

### Voxel clustering for enhanced detection

In contrast to previous approaches that estimate spine volume from the spine tip backward toward the dendrite (Rodriguez et al., 2008), Spine Detector identifies potential spine voxels at the dendrite shaft and estimates their volume by iteratively adding layers of connected voxels toward the spine tips. To quickly estimate the minimum distance between each voxel and the nearest dendrite surface, Spine Detector uses the radius of each node across the neuron trace as a representation of the dendrite surface and performs a distance transform on the image (Figure S2F). The initial seeds of potential spines are the voxels the shortest distance from the dendrite surface. In each iteration, potential spines are identified and grown by adding new layers of connected neighbor-voxels until a spine edge is detected. This is achieved by establishing a floor value to the distance between the initial seeds and the dendrite surface and repeatedly adding layers of connected neighbor-voxels equal to the floor value of the previous layer. At the end of each iteration, Spine Detector determines whether the number of voxels have exceeded the user-defined spine size and whether the maximum layer width has exceeded the user-defined layer width. If the most recently added layer did not meet these criteria, all previous layers are discarded and the voxels in that layer serve as the seed for the next layer. The iteration stops when all qualified voxels are assessed. Spine candidates are rejected based on user-supplied parameters for minimum voxel count and minimum spine length, allowing users to reconstruct images acquired at different magnifications. Notably, spines can be detected with this methodology regardless of the resolution of the spine neck.

### Intensity-based segmentation of adjacent spines

Limited image resolution, inaccurate thresholding, and physical proximity can all give rise to adjacent spines incorrectly categorized as a single synapse. Based on the observation that spine voxel intensities are naturally brighter at the center than the edges, we adopted an adapted watershed algorithm to separate spines within close spatial proximity (Barnes et al., 2014). First an initial threshold is set at a relatively high fluorescence intensity so that only the center-voxels of spines are identified (Figure S2G). With the successively decreasing fluorescence toward the spine border, the spine boundary grows in size. When two potential spine boundaries meet they each become defined to separate adjacent spines. The merger of two spine volumes is only considered when both spines are relatively small (lower than 1% of the average volume).

### Inhibitory synapse detection

We labeled inhibitory synapses using the scaffolding protein Gephyrin tagged with a fluorescent protein as a marker (Chen et al., 2012). Because these synapses can only occur on the dendrites or the spines of neurons of interest, we use the image from the cell-fill channel containing the dendrites and the spines as a mask image to extract the relevant region for the inhibitory synaptic marker. Then, signal beyond user-input parameters for minimum/maximum voxel count and distance from the trace is excluded and potential inhibitory synapses from the resulting image are identified based on a user-input intensity threshold. Users have the ability to accept or reject potential inhibitory synapses, adjust their volume, and assign them as dendrite-targeting or spine-targeting.

### Stitching neuron traces across serial 3D image sections

To assemble the neuron reconstructions traced across multiple image stacks we used Neuron Stitcher (Chen et al., 2017), a software suite for stitching non-overlapping neuron fragments in serial 3D image sections. The software identifies severed neurite traces at the section planes, known as 'border tips', and then uses a triangle matching algorithm to align traces created from neurons spanning serial tissue sections. Once the initial border tip matches are identified, the alignment is estimated in the form of an affine transformation and the border tips are connected to form a complete neuron trace.

### Neurite subtyping

To better understand the synaptic distribution within domain and segment levels, we developed the Subtree Labeling program as a plug-in of Vaa3D to subtype neurites for further analysis. Using this program it is possible to assign a neurite segment into multiple categories: axon, soma, apical trunk, apical tufts, apical oblique dendrites, and basal dendrites. The user interface allows the user to select the starting vertex for each branch and to assign neurite type. The program first finds the tree node for soma and sorts the tree with the soma node as the tree root. Then, all the child vertices of the starting vertex are assigned the same branch type as each manually annotated starting vertex.

### User's guide

#### *Synapse Detector Interactive User Interface*

To broaden the utility of SynapseDetector to work with a variety of different data acquisition processes, we designed an interactive interface to (1) allow visual evaluation of detection results and accept or reject putative synapses; and (2) enable manual correction of synaptic volume through addition or subtraction of associated pixels. The software was implemented in C/C++ as a plugin of Vaa3D, which is a publicly available open source platform with a user-friendly interface for 3D+ image analysis and visualization. In the following sections, we will introduce how to use the tools. For detailed directions how to create neuron traces using Vaa3D, see the recently published protocol (Peng et al., 2014).

Main website: http://home.penglab.com/proj/vaa3d/
Documentation: https://github.com/Vaa3D
Help/Discussion Forum: https://www.nitrc.org/forum/forum.php?forum_id=1553
Bug tracking and requesting new features: https://www.nitrc.org/tracker/?group_id=379

#### *Sorting dendrite traces for reconstruction*

A dendrite trace (swc file) is composed of a series of connected nodes with varying radii. This plugin connects nodes that were not linked during manual trace editing, which is critical for proper segment classification. This plugin allows the user to designate the soma as the "root node," the first node in the tree from which the distance to all daughter nodes can be determined to analyze synaptic distribution.

1. In Vaa3D, drag a neuron trace into the 3D viewer.
2. Use 'Cmd/Ctrl+L' to toggle between the line (skeleton) display mode and the surface mesh display mode of the neuron. In line display mode it is possible to visualize root nodes contained within the trace.
3. If the trace contains a soma, hover cursor over soma to identify the node number that will be designated as the root node.
4. In Vaa3D, go to the 'Plug-in' main window menu and click 'neuron_utilities', then click on 'sort_neuron_swc', and finally click on 'sort_swc'.
5. Select the trace in the 'Open from 3D Viewer' tab.
6. If the trace contains a soma, specify the root node number as the soma node number. If the trace does not contain a soma, click 'cancel'.
7. Specify a voxel threshold for adjacent segments to be connected. To connect all segments click 'cancel'. Save the sorted neuron trace.

#### *Resampling dendrite traces for reconstruction*

To maximize the spatial resolution of synaptic distribution analysis, it is recommended to resample the associated neuron trace to contain the highest possible number of tree nodes.

1. In Vaa3D, go to the 'Plug-in' main window menu and click 'neuron_utilities', then click on 'resample_swc', and finally click on 'resample'.
2. Select the trace and specify a step length of 1. Click 'ok' and save the resampled neuron trace.

### *Using Crop Image Trace to analyze large image volumes*

This new tool allows the user to analyze image volumes with Synapse Detector that would normally be too large by cropping a region of interest based on XYZ pixel coordinates and aligning an associated neuron trace to the resulting image volume. In practice, image volumes greater than 2000 × 2000 pixels in X and Y and 500 pixels in Z are difficult to reconstruct without cropping.

1. In Vaa3D, use 'Cmd/Ctrl+O' to open the appropriate image file.
2. In the tri-view window, click 'see in 3D' and then click 'entire image' to visualize the image file.
3. Drag and drop the neuron trace corresponding to the image file into the 3D view window.
4. Go to the 'Plug-in' main window menu and click 'image_geometry', and then 'crop_image_tace', and finally click on 'crop'.
5. Select an appropriate output directory, and specify the XYZ coordinates to crop the image (the number of pixels in X, Y, and Z that compose each image can be viewed in the tri-view window and 3D viewer), and specify the color channels to include in the new image. Click on 'run and save'.

### *Synapse annotation with Synapse Detector*

This new tool semi-automatedly identifies dendritic spines (Spine Detector) or inhibitory synapses (IS Detector) and quantifies their morphology and spatial distribution. Synapses can be manually accepted or rejected, as well as edited by dilating or eroding pixels. IS Detector also allows the user to designate inhibitory synapse location on either a spine or the dendritic shaft.

#### *Spine Detector user interface*

1. In Vaa3D, go to the 'Plug-in' main window menu, click 'synapse_detector', and click on 'SpineDetector_NewProject'. Users can also continue an existing project by clicking 'SpineDetector_ExisitingProject'.
2. Load the image volume (v3dpbd or v3draw), associated trace file (swc), and designate an output destination for the sorted reconstruction. Select the color channel of the cell-fill.
3. Specify the threshold for background signal in the image and volume parameters for potential spines. Pixel to micron conversion can be calculated from the imaging magnification and is usually stored within the image properties. Click 'Run'.
4. Click 'Proofread by segment' to edit spines along a dendrite segment (recommended) or 'Proofread by spine' to edit each spine individually.
5. Accept/reject potential spines and proofread spine morphology by dilating/eroding volume. The highlighted regions indicate the potential spines (Figure S1C). It is recommended to look at the segment at different angles and toggle between views with the spine annotation channel on and off in the 3D viewer.
6. Click 'Save current result' to save intermediate results during proofreading. Spine Detector will generate 4 files in the output folder: a text file 'project.txt' (includes all info needed to reload the last saved reconstruction project), a marker file indicating the positions of accepted/rejected spines, a csv file (table of accepted spine information), and an image file of accepted spines.
7. Click 'Finish proofreading' to save final results after proofreading. After proofreading is completed, Spine Detector generates 2 image files (edited spine reconstruction and isolated spine annotations), a marker file of spine positions, and a csv file containing spine morphology data (all data measured in pixels).

#### *IS Detector user interface*

1. In Vaa3D, go to the 'Plug-in' main window menu, click 'synapse_detector', and click on 'IS_Detector_NewProject'. Users can also click on 'IS_Detector_ExisitingProject' to reload a previously saved project.
2. Load the image volume (v3dpbd or v3draw), associated trace file (swc), and designate an output destination for the sorted reconstruction. Select the color channel of the cell-fill and the color channel of the inhibitory synaptic marker (or other punctate intracellular marker).
3. Specify the threshold for background signal in both image channels and volume parameters for potential inhibitory synapses. Pixel to micron conversion can be calculated from the imaging magnification and is usually stored within the image properties. Click 'Run', and then click 'Proofread by segment'.
4. Accept/reject potential inhibitory synapses and proofread morphology by dilating/eroding volume and specifying synapse location on spine/dendrite. The highlighted regions indicate the potential inhibitory synapses (Figure S1D). It is recommended to adjust the lookup table thresholds for synaptic visualization by clicking the 'Vol Colormap' button on the right-side control pane of the 3D viewer.
5. Click 'Save current result' to save intermediate results during proofreading. Spine Detector will generate 2 files in the output folder: a text file (includes all info needed to reload the last saved reconstruction project) and a csv file (table of accepted spine information).
6. Click 'Finish proofreading' to save final results after proofreading. After proofreading is completed, Spine Detector generates 2 image files (unedited and edited inhibitory synapses), a marker file of synaptic positions, and a csv file containing synaptic morphology data (all data measured in pixels).

### *Embedding synaptic data within the neuron trace*

After spines and inhibitory synapses have been annotated throughout the image volume, synaptic information stored in tables can be associated with their corresponding nodes throughout the neuron trace using the Synapse Detector Combiner.

1. In Vaa3D, go to the 'Plug-in' main window menu click 'synapse_detector', and click on 'Combiner'.
2. Load the spine and inhibitory synapse tables that correspond to the neuron trace. If the image volume was cropped before reconstruction the trace will be associated with tables from each cropped region. Click 'Run', and save the neuron reconstruction.

### *Assembling reconstruction fragments with Neuron Stitcher*

For directions how to stitch neuron traces using Neuron Stitcher, see the recently published protocol (Chen et al., 2017). To store synaptic information in the final reconstruction, assemble eswc traces.

### *Annotating reconstruction traces with Subtree Labeling*

This new tool creates an enhanced neuron skeleton that contains information about dendrite identity, branch order, and cumulative dendritic distance from the soma. The user interface allows the user to select the starting vertex for each branch and to assign neurite type. Child vertices of each starting vertex are assigned the same branch type as each manually annotated starting vertex. To label neuron reconstructions stitched from multiple fragments throughout the entire dendritic arbor, these traces must first be sorted with the Neuron Connector plugin to preserve the eswc file type.

1. In Vaa3D, go to the 'Plug-in' main window menu, click 'neuron_utilities' and 'neuron_connector', and select 'connect_neuron_swc'.
2. Load the input trace file and designate an output destination for the sorted reconstruction.
3. Set the 'connection configuration' to 'connect all, shortest distance and click 'Connect'.
4. After sorting the reconstruction, drag it into the 3D viewer.
5. Use 'Cmd/Ctrl+L' to toggle between the line (skeleton) display mode and the surface mesh display mode of the neuron. In line display mode it is possible to visualize root nodes contained within the trace.
6. Right-click at the soma to and click 'create marker from the nearest neuron-node' to create a marker at the root node. Create markers between the root node and dendrite terminals according to experiment-specific labeling schemes (Figure S1E).
7. In Vaa3D, go to the 'Plug-in' main window menu, click 'neuron_utilities', and then 'subtree_labeling'.
8. Select 'Refresh markers' to ensure all markers were selected. Assign dendrite labels to each marker. It is possible to add new markers and click 'Refresh markers' to add them to the list of labeled markers. Markers will be labeled in descending order starting with marker 1, so it is recommended to place makers from the root node outward according to the labeling scheme.
9. Click 'run labeling'. Review the neuron trace in the 3D viewer to verify segments were properly labeled and click 'save' within the Subtree Labeling interface window.

## Synaptic map visualization

### *Heatmap generation*

We query the synaptic annotations for individual neurons to return a subset of the synapses satisfying the query. Some examples are "all inhibitory synapses," "large spines," and "all inhibitory synapses on spines." We classified "large" synapses as greater than the 20$^{th}$ percentile of synaptic volume for each neuron, closely corresponding to the persistent 160% increase in volume reported for synapses following structural forms of long-term potentiation (Harvey and Svoboda, 2007; Matsuzaki et al., 2004; Petrini et al., 2014). We calculate the path distances between these nodes and the soma, which is the 3D distance on the dendritic arbor from the soma to the node of interest. We calculate the distances between consecutive nodes that are in "ancestor-descendent" relationships on the neuronal arbor by obtaining the absolute value of the difference between their path distances.

To calculate the density of the synapses of interest at any given point on the dendritic arbor (the heatmap), we count the synapses of interest that are within W μm of that point in terms of the path distance on the dendritic arbor, and convert these counts into color codes. Smaller W values increase the resolution of the heatmap. On the other hand, when W is too small, the heatmap will display high frequency noise. Therefore, we set the W values adaptively for each dendritic arbor as

$$W = \min(8 / \lambda, 100)$$

$$\lambda = |S|/L$$

where |S| denotes the number of synapses of interest, and L denotes the total dendritic length of the arbor so that the unit of λ is $\mu m^{-1}$. When mapping local counts to colors in the heatmaps, we typically saturate the range of counts between the 2$^{nd}$ and 98$^{th}$ percentiles of the values to utilize the dynamic range of the colors more effectively.

### *E/I balance heatmap generation*

The excitatory and inhibitory heatmap values for individual neurons are scaled and shifted to lie in the *[0, 1]* interval. The absolute value of the difference, which again lies in the *[0, 1]* interval, is displayed.

## Synaptic distribution analysis

### *Within-domain randomization for structural organization analysis*

For each neuron, we first find all the nodes of the arbor trace in the domain of interest. The nodes that carry synapses on them have extra annotations reflecting the size and type of the synapses. Then, we reassign the size-and-type annotations to those nodes uniformly at random, thus leaving the structure of the arbor unchanged.

### *Branch-level synaptic rate correlation analysis*

For each relevant branch (i.e., primary, intermediate, terminal) in each neuron, we count the synapses of interest and divide by the path length of that branch to obtain the density estimate. We calculate the correlation coefficient and the *p-value* pair for each plot using the *corrcoef* command in MATLAB. For E/I synaptic density correlation plots, segments without either E or I synapses were excluded.

### *Quantification and statistical analysis of synaptic distribution data*

Dendritic domain data are shown as the mean ± SEM of reconstructed neurons, unless otherwise stated. D'Agostino and Pearson normality tests were used to confirm that datasets fit Gaussian distributions. t tests were used to compare the mean of two groups with corrections for multiple comparisons: discovery determined using the Two-stage linear step-up procedure of Benjamini, Krieger and Yekutieli, with Q = 1%. A one-way repeated-measures ANOVA with Tukey's test for multiple comparisons was used when more than two groups existed. Significance for all experiments was placed at $p < 0.05$. Statistical tests were carried out with GraphPad Prism.

## Modeling

### *Passive neuron model with synaptic input*

Reconstructed morphological data, synaptic attributes and spatial distribution of E and I synapses were taken from Vaa3D reconstructions. Specific membrane resistance and capacitance, and axial resistance were 12,000 $\Omega cm^2$, 1 $\mu F/cm^2$, 150 $\Omega cm$ respectively. These values were chosen such that the somatic input resistance and time constant will be within known biological ranges for these neurons 92 ± 15MΩ and 12ms, respectively (Sarid et al., 2007)). The activation of excitatory and inhibitory synapses was aimed to replicate *in vivo*-like input to cortical neurons (Tremblay et al., 2016). Toward this end the synapses were activated in a temporally- and spatially- structured fashion. 90% of the E synapses were served as the background activity; they were randomly selected over the dendritic surface and activated following homogeneous Poisson process with an average rate of $\lambda = 1.75$ Hz. The other 10% of the E synapses represent the "sensory" excitation, activated following an inhomogeneous Poisson process that is modulated at 10 Hz, with a time-dependent rate, $\lambda(t)$, ranging between 0 and 3.5 Hz, leading to an average input rate of 1.75 Hz. In Figure S7A, the activations of all excitatory and inhibitory synapses were sampled from homogeneous Poisson processes with an average rate of 1.75 Hz and 10 Hz respectively. For the comparison of constant conductance and synapse volume informed conductance in Figures S7B and SC, we have modified the conductances of excitatory synaptic conductance to be (spine head volume * 0.4nS / spine head volume mean), and the inhibitory synaptic conductance to be (bouton volume * 1.0nS / bouton volume mean), where the mean is the mean over the entire population of synapses. This allowed us to keep the average synaptic conductance the same, while varying the specific conductance based on the synaptic volume.

Inhibitory synapses targeting the soma and the primary basal branches represent "feedforward" inhibition. These synapses were activated following an inhomogeneous Poisson process that is modulated at 10 Hz and phase-locked to the "sensory" input oscillations with $\lambda(t)$, ranging between 0 and 20 Hz, leading to an average input rate of 10 Hz. Inhibitory synapses targeting the terminal basal and apical branches represent the "feedback" inhibition; these synapses were activated following an inhomogeneous Poisson process that is modulated at 10 Hz with 15 ms delay with respect to the "sensory" input oscillations, with $\lambda(t)$, ranging between 0 and 20 Hz, leading to an average input rate of 10 Hz. The rest of the inhibitory synapses served as the background inhibition they were activated following homogeneous Poisson process with an average rate of $\lambda = 10$ Hz. This combined synaptic input generated a mean somatic firing rate for the 10 modeled neurons of 4.6 ± 3.6 Hz, similar to that found experimentally (O'Connor et al., 2010). The synaptic peak conductance for the E synapses was 0.4 nS (for α-amino-3-hydroxy-5-methyl-4-isoxazolepropionic acid (AMPA) component as well as for the N-methyl-D-aspartate (NMDA) components) and 1 nS for the γ-Aminobutyric acid ($GABA_A$) synapses. The rise time constants for the conductances of these synapses was 0.2 ms, 2.04 ms and 0.18 ms, respectively and the respective decay time was 1.7 ms, 75.2 ms and 1.7 ms. The reversal potential values are 0 mV, 0 mV, and −80 mV, respectively. Dendritic voltage traces were recorded from the center of the respective dendritic branch. Modeling and simulation was performed using NEURON simulator, accessed using a python script (Carnevale and Hines, 2006).

### *Active neuron model*

Active membrane ion channels were taken from the Blue Brain Project models of L2/3 PNs (Markram et al., 2015) and tuned to produce similar results to that found *in vivo* for L2/3 PNs (Waters et al., 2003). To ensure that our model captures important aspects of dendritic nonlinearities and voltage attenuation, we tuned the $Na^+$ and $I_h$ membrane conductances to replicate two experiments as in Waters et al., 2003. In order to replicate the attenuation of the back-propagating action potential along the apical trunk in L2/3 PN as in Figure 6C, a step depolarization current of 200 pA for 200 ms was injected to the modeled soma, invoking a somatic action potential, and recorded the amplitude at 10 microns intervals along the apical trunk (Figure 6D). To replicate the contribution of $Na^+$ channels to the backpropagation of action potentials (Figure 6E), we have injected 200 pA for 200 ms to the soma, invoking an action potential, and recorded the voltage both at the soma and 80 microns from the soma on the apical trunk. Then, we simulated

the application of TTX by removing the $Na^+$ channels from the model, voltage clamping the soma to the voltage trace created by the action potential, and recording the amplitude of the passively propagated action potential 80 μm from the soma on the apical trunk (Figure 6F). The model (Figures 6D and 6F) was able to replicate the experimental results (Figures 6C and 6E) of both the attenuation and the dependency on $Na^+$ channels of the back-propagating action potential.

***Changing E/I ratio variance across dendritic domains***

To study the influence of the ratio of excitatory and inhibitory synapses in a given dendritic branch, we iteratively increased or decreased the variance of E/I ratios over all branches belonging to a given domain. To change the E/I ratio variance, we randomly distributed the location of synapses between branches, while keeping the total number of synapses in the domain fixed (as found experimentally for the respective modeled neuron). This process was repeated ten times, each time with a different initial distribution of the synapses. In Figures 7D and 7E and Figure S6 the voltage time integral (in a time window of 3000 s) was computed at the center of each branch in a particular domain, for different E/I SD, averaged over all branches in that domain. The same was performed for the somatic firing rates (Figure 7F) for different E/I SD in the basal terminal domain.

***Contribution of domain-specific synapses to the voltage in that domain***

To measure the contribution of synapses located in a specific domain to the depolarization in that domain, we simulated each of the modeled neuron with excitatory and inhibitory synapses as described above, and calculated the mean voltage time-integral in each domain. We then calculated the respective mean voltage time-integral when all synapses in that domain were not active and compared the two cases (Figure S7D).

## DATA AND CODE AVAILABILITY

The Synapse Detector tools we present here are available as part of the free and open source morphology reconstruction platform Vaa3D (vaa3d.org). The 12 synaptic maps of L2/3 pyramidal neurons from primary somatosensory cortex analyzed in this study are available in the supplementary materials. The software used to generate the heatmaps, the rate plots, and the within-domain randomization results is available at https://github.com/uygarsumbul/spines. The computational firing models generated in this paper are available at https://senselab.med.yale.edu/modeldb/enterCode?model=261460.